Applied Energy 417 (2026) 128051

Contents lists available at ScienceDirect

Applied Energy

journal homepage: www.elsevier.com/locate/apen

Long-term degradation and microstructural evolution of industrial-sized solid oxide electrolysis cells operated in co-electrolysis for power-to-X applications

Daniel Reiner[a,*], Srđan Marković[a], Hartmuth Schröttner[b,c], Pavle Boškoski[d,e], Christoph Hochenauer[a], Vanja Subotić[a]

[a] Institute of Thermal Engineering, Graz University of Technology, Inffeldgasse 25/B, 8010 Graz, Austria
[b] Institute of Electron Microscopy and Nanoanalysis (FELMI), Graz University of Technology, Steyrergasse 17, 8010 Graz, Austria
[c] Graz Centre for Electron Microscopy (ZFE), Steyrergasse 17, 8010 Graz, Austria
[d] Jožef Stefan Institute, Department of Systems and Control, Jamova cesta 39, SI-1000 Ljubljana, Slovenia
[e] Faculty of Information Studies, Ljubljanska cesta 31a, 8000 Novo mesto, Slovenia

HIGHLIGHTS

- Industrial-sized SOECs evaluated under PtX-relevant co-electrolysis gas compositions.
- Pt from electric contacting enhanced performance in early stages of operation.
- Degradation quantified with EIS, DRT, and post-mortem analysis (SEM + EDX & Raman).
- Fuel-electrode degradation mainly due to Ni–YSZ functional-layer coarsening.
- Air-electrode degradation increased by reduced air flow and related surface changes.

GRAPHICAL ABSTRACT

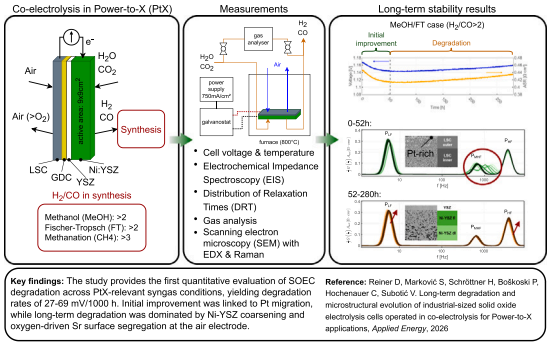

ARTICLE INFO

Keywords:
Co-electrolysis
Power-to-X (PtX)
Solid oxide electrolysis cell (SOEC)
Electrochemical analysis
Distribution of relaxation times (DRT)
Scanning electron microscopy (SEM)

ABSTRACT

Solid oxide electrolysis cells (SOECs) are central to high-efficiency Power-to-X (PtX) pathways, yet quantitative data on their long-term stability under application-relevant co-electrolysis conditions remain rare. This study provides a systematic evaluation of SOEC degradation under syngas targets representative of methanol synthesis, Fischer-Tropsch synthesis ($H_2/CO = 2$), and methanation ($H_2/CO = 3$), using industrial-sized, fuel-electrode-supported planar cells (81 cm^2). The cells were operated at 800 °C and elevated current densities of 750 mA/cm^2 for up to 500 h. Performance evolution was monitored by voltage and temperature measurements, incremental electrochemical impedance spectroscopy (EIS), distribution of relaxation times (DRT), and outlet-gas analysis. Post-mortem SEM/EDX analysis (surface & cross-section) linked electrochemical degradation with microstructural changes. The key findings of this work are: The cells exhibited an initial improvement phase, with voltage reductions of up to 3.5%, associated with enhanced oxygen surface exchange at the air electrode, consistent with Pt migration from the contacting mesh, followed by degradation. In all operating scenarios, the dominant fuel-electrode degradation mechanism is the coarsening of the Ni-YSZ functional layer, which decreases porosity and increases diffusion-related losses. In the $H_2/CO = 2$ case, the use of only half the air-flow

* Corresponding author.
Email address: daniel.reiner@tugraz.at (D. Reiner).

https://doi.org/10.1016/j.apenergy.2026.128051
Received 1 December 2025; Received in revised form 17 March 2026; Accepted 7 May 2026
Available online 17 May 2026

rate applied in the $H_2/CO = 3$ case increased the local oxygen partial pressure, which led to more pronounced Sr surface segregation and partial air-electrode degradation. Corresponding voltage degradation rates were 68.7 and 27.3 mV/1000 h, with ASR degradation of 92 and 36 mΩcm^2/1000 h, the latter increasing at extended operating times. These results provide a quantitative analysis of SOEC degradation under PtX-relevant syngas conditions and highlight operating factors influencing stability during industrially relevant co-electrolysis.

1. Introduction

The growing share of wind and solar power in many regions has intensified the need for technologies that can store excess renewable electricity and convert it into chemical energy carriers. According to recent reports by the International Energy Agency (IEA), renewables supplied more than 32% of global electricity in 2024 and are projected to exceed 40% by 2030 [1]. Similar trends reported by IRENA [2,3] and Ember [4] highlight that the rapid expansion of wind and solar, together accounting for over 95% of new renewable capacity additions, continues to drive demand for flexible conversion and storage pathways. Power-to-X (PtX) concepts offer a particularly promising solution, enabling intermittent electricity to be transformed into fuels and feedstocks that can be integrated into existing industrial value chains. High-temperature solid oxide electrolysis cells (SOECs) are especially attractive, achieving electrical efficiencies of 70–85% because part of the required energy can be provided as heat, surpassing typical efficiencies of low-temperature electrolysis technologies [5–7]. A key advantage of SOECs is their ability to convert mixtures of H_2O and CO_2 directly to syngas via co-electrolysis, avoiding a separate reverse water-gas shift step and enabling simpler thermal integration with downstream chemical synthesis. In this context, SOEC-based co-electrolysis has increasingly been discussed as a versatile platform for integrated energy and chemical conversion, enabling flexible CO_2 utilization and direct coupling to downstream synthesis routes. Recent comprehensive reviews further emphasize the system-level potential of such high-temperature electrochemical reactors for sector coupling and compositionally tunable syngas production [8]. At the fuel electrode, H_2O and CO_2 are reduced to H_2 and CO according to Eqs. (1) and (2) [7,9]. In addition to these electrochemical pathways, the gas mixture is influenced by the reverse water–gas shift (RWGS) equilibrium (Eq. 3), which interconverts H_2, CO_2, CO, and H_2O in the cell environment. The oxygen ions formed at the fuel electrode are transported through the electrolyte and released as molecular oxygen at the oxygen electrode (Eq. 4). Taken together, these coupled reactions determine both the syngas composition produced during co-electrolysis and the associated thermal demand of the process.

$$H_2O + 2e^- \rightleftharpoons H_2 + O^{2-} \quad \Delta_R H_m^{800} = 1179\ \text{kJ/mol} \tag{1}$$

$$CO_2 + 2e^- \rightleftharpoons CO + O^{2-} \quad \Delta_R H_m^{800} = 1213\ \text{kJ/mol} \tag{2}$$

$$H_2 + CO_2 \rightleftharpoons H_2O + CO \quad \Delta_R H_m^{800} = 34\ \text{kJ/mol} \tag{3}$$

$$O^{2-} \rightleftharpoons 0.5\,O_2 + 2e^- \quad \Delta_R H_m^{800} = -931\ \text{kJ/mol} \tag{4}$$

Co-electrolysis is therefore central to several major PtX routes, including methanol synthesis (I), Fischer-Tropsch synthesis of synthetic fuels (II), and synthetic methane production via catalytic methanation (III) (see Fig. 1). Each process requires a characteristic syngas composition, which in turn dictates specific SOEC operating conditions. Fischer-Tropsch synthesis typically demands a H_2/CO ratio near or slightly above 2 [10,11], while methanol synthesis commonly targets a similar value [12,13]. In contrast, methanation requires substantially more hydrogen, with stoichiometric $H_2/CO = 3$ [14,15]. In this study, we therefore selected two representative H_2/CO ratios corresponding to three PtX pathways to examine how route-specific gas compositions and operating conditions influence SOEC performance and long-term stability. These distinct requirements provide an ideal basis for evaluating the interplay between gas composition, degradation behavior, and cell architecture under industrially relevant operation.

While numerous studies have investigated SOEC degradation mechanisms [16–18], most have been conducted under simplified laboratory conditions or model gas compositions that are not directly linked to specific Power-to-X (PtX) applications. In practical PtX systems, however, the required H_2/CO ratio determines not only the inlet gas composition but also the steam-to-carbon ratio, reactant utilization, air-flow management, and thermal balance of the system. These operational parameters influence oxygen chemical potential, local electrode polarization, and mass-transport processes, which are known to affect degradation mechanisms such as Ni coarsening in the fuel electrode and Sr surface segregation in the air electrode [19,20]. Therefore, a systematic evaluation of industrial-sized SOECs under application-driven

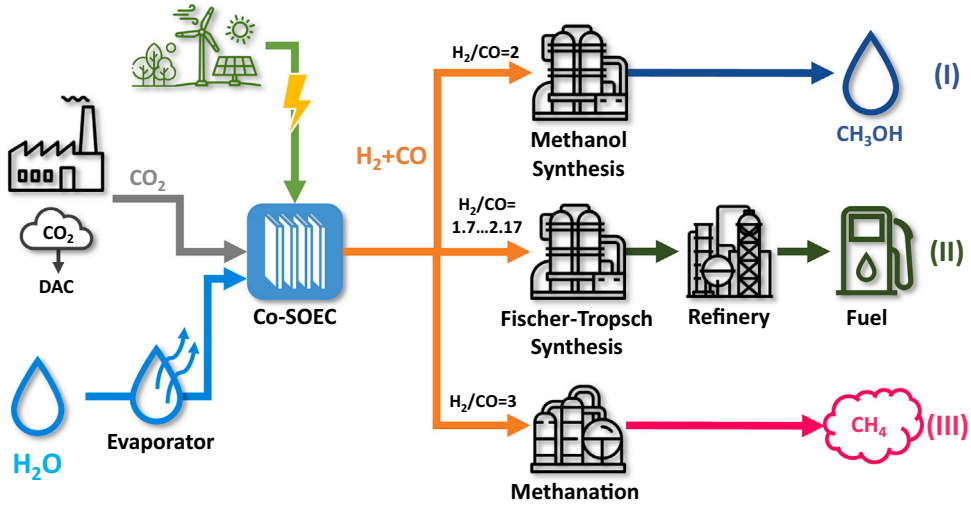

Fig. 1. Application paths considered for syngas from co-electrolysis: (I) methanol synthesis, (II) Fischer-Tropsch synthesis, (III) methanation.

syngas targets is essential to understand how realistic operating constraints influence long-term stability. Such knowledge is critical for bridging the gap between mechanistic degradation studies and reliable industrial implementation of SOEC-based PtX systems. Despite these application-driven requirements, the durability of SOECs under realistic co-electrolysis conditions is still not fully resolved [21–23]. In parallel, significant efforts have been devoted to the development of advanced fuel-electrode materials to improve stability during co-electrolysis. For example, high-entropy alloy-based fuel electrodes have recently been proposed to enhance CO selectivity and oxidation resistance under electrolysis conditions [24]. Most SOEC single cell durability studies have been carried out on button cells or other small-scale cells operated under conditions that are often set specifically to trigger particular degradation mechanisms. While such experiments have provided important insights into phenomena such as Ni particle coarsening [25], Ni-migration in Ni-YSZ [26], and oxygen-electrode degradation [27], they do not necessarily reflect the application conditions encountered during actual co-electrolysis operation. Therefore, laboratory setups designed to reproduce more realistic boundary conditions for industrial-sized single cells are needed to obtain a representative picture of degradation under practical operating environments (e.g., realistic temperature distributions and air-flow management).

To date, only limited experimental work has been published on industrial-size SOEC single cells operated for extended periods under gas compositions and conditions representative of specific PtX applications. These studies focus either on accelerated stress conditions, or simplified model gas mixtures, which do not fully capture the coupled effects of syngas composition, air-flow management, and thermal balance encountered in industrial operation. Wolf et al. [18] investigated steam and co-electrolysis to compare both modes and distinguish the degradation. They reported a voltage degradation rate of 16%/1000 h (40% H_2O + 40% CO_2 + 20% H_2) and observed Ni-agglomeration and depletion on the fuel electrode. Hyeon-Ye et al. [28] infiltrated the fuel electrode with Pd/Fe-catalysts to improve the conversion of CO_2 and achieved a voltage degradation rate of less than 1%/100 h (10%/1000 h). Unachukwu et al. [29] compared the degradation steam and co-electrolysis (40% H_2O + 40% CO_2 + 20% H_2) and observed a lower degradation rate for co-electrolysis of about 26%/1000 h. Tao et al. [17] reported degradation rates at higher current densities at 1500 mA/cm^2 for 15%/1000 h and at 2000 mA/cm^2 for 30%/1000 h in co-electrolysis with the degradation mainly due to microstructural changes in the Ni-YSZ electrode close to the YSZ electrolyte. But none of the aforementioned researchers investigated the long-term stability of industrial-sized cells in co-electrolysis in realistic operation environments. This lack of available data makes it difficult to assess how commercial cells behave in practice and what types of degradation dominate under co-electrolysis operation with industrially relevant syngas targets. This highlights the necessity to fully understand the underlying processes and mechanisms in application conditions. This study aims to address this gap. Commercial, industrial-scale fuel-electrode-supported single cells (Ni-YSZ/YSZ/GDC/LSC) with an active area of 81 cm^2 were operated under two co-electrolysis scenarios representative of specific PtX routes (Fig. 1). The experiments were conducted under realistic thermal boundary conditions, feed-gas compositions, and operating modes to achieve the required H_2/CO ratios at the cell outlet. A central objective of this work was to quantify degradation rates of industrial-sized SOEC single cells under operating environments directly tailored to distinct PtX applications, thereby providing application-relevant durability data currently limited in the literature. Cell performance was monitored over time through voltage and temperature measurements, combined with incremental electrochemical impedance spectroscopy (EIS) and distribution of relaxation times (DRT) analysis to elucidate the underlying degradation mechanisms. Post-mortem characterization using scanning electron microscopy (SEM) in combination with energy-dispersive X-ray spectroscopy (EDX) was carried out and compared with a reference cell in its reduced state. This integrated approach enables a direct link between the observed degradation features and the operating conditions characteristic of each PtX route. The results provide practical insight into how commercial SOEC single cells perform under realistic co-electrolysis environments and identify the dominant degradation pathways associated with the selected PtX applications. These findings can support future optimization of operating strategies and system-level integration for industrial Power-to-X implementation.

The main contributions of this work are summarized below:

- *Application-driven long-term evaluation*: Systematic degradation assessment of industrial-sized SOEC single cells operated under PtX-relevant co-electrolysis conditions targeting methanol/Fischer–Tropsch and methanation syngas compositions.
- *Integrated diagnostic approach*: Combination of galvanostatic operation, fast EIS, DRT analysis, and post-mortem SEM/EDX to correlate electrochemical performance with microstructural evolution.
- *Electrode-specific degradation analysis*: Identification of dominant fuel- and air-electrode degradation pathways under distinct PtX-relevant operating conditions, linking electrochemical signatures to microstructural changes.

Accordingly, this work investigates not only performance differences between two syngas targets, but more fundamentally how application-specific operating requirements influence degradation pathways in industrially relevant SOEC configurations.

2. Experimental

This section offers a detailed overview of the experimental configuration, the analytical techniques applied during the study, and a thorough description of the test rig used.

2.1. Description of planar single cells & SOEC test rig

In this study, industrial-scale fuel electrode-supported cells were experimentally examined. The total area of each cell was 10×10 cm^2, with an active fuel electrode area measuring 9×9 cm^2. The tested cells, also known as elcoCell® ASC-300C, were commercially sourced from ©Elcogen AS [30]. The cells under consideration consisted of a Ni-based cermet (Ni/YSZ) fuel electrode with a thickness of approximately 294 µm, a Yttria-Stabilized Zirconia (YSZ) electrolyte layer with a thickness of approximately 6 µm, and a lanthanum strontium cobaltite (LSC) air electrode incorporating a gadolinium-doped ceria (GDC) barrier layer with a total thickness of approximately 15 µm of LSC and GDC combined. The total thickness of the cell is determined by the sum of all layers, yielding a final measurement of approximately 315 µm. The solid oxide electrolysis cell (SOEC) was mounted within a custom ceramic housing designed to facilitate temperature monitoring across the active electrode area. A total of twelve thermocouples (TCs) were strategically positioned in close proximity to both the fuel and air electrodes of the cell, as depicted in Fig. 2. The placement of six thermocouples on each side, at the fuel and air electrode, within the active region was conducted on a plane parallel to the cell surface. This is illustrated using dashed outlines and a transparent overlay. The precise locations of each thermocouple have been documented in a previous publication [31]. The experiments were conducted under a co-flow gas

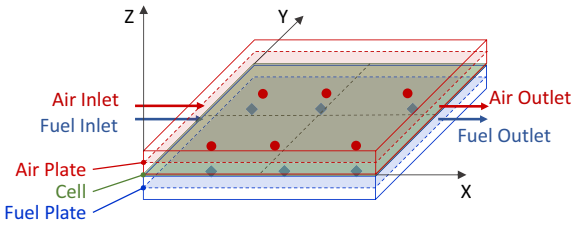

Fig. 2. Positions of thermocouples over the active cell area in 3D [31].

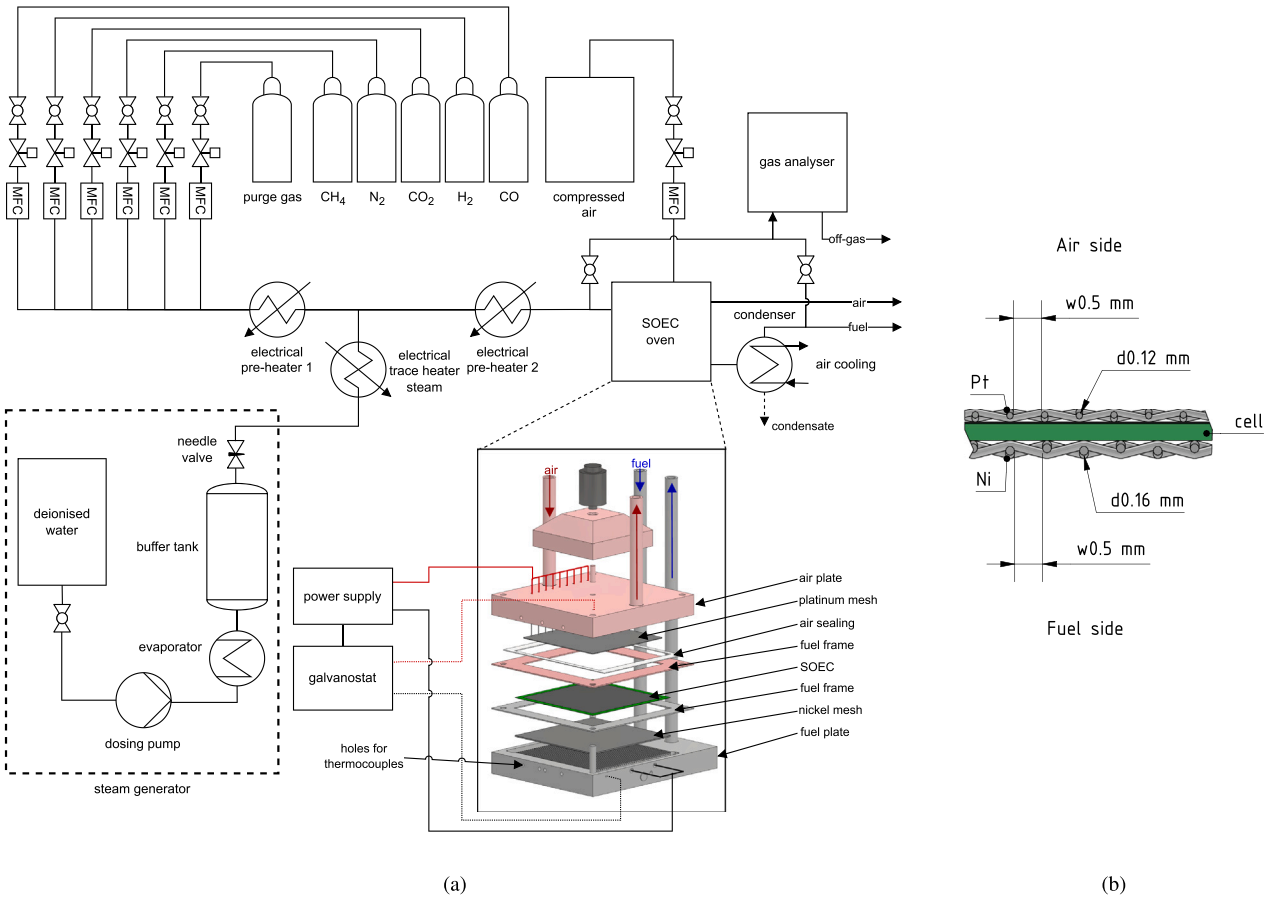

Fig. 3. Scheme of the used SOEC test rig. (a) overall experimental setup [31]. (b) Schematic cross-section of the single-cell contacting configuration, illustrating the platinum mesh on the air electrode side and the nickel mesh on the fuel electrode side within the ceramic housing. The fuel electrode was supplied with the respective co-electrolysis gas mixtures as specified in Table 1, while the air electrode was fed with compressed air (21% O_2 in N_2), which was reduced to atmospheric pressure prior to entering the cell.

configuration. Electrical current collection on the air electrode was realized using a platinum mesh (wire diameter 0.12 mm, width 0.5 mm, 260 meshes/cm^2) placed directly on the LSC surface. On the fuel electrode side, a nickel mesh (wire diameter 0.16 mm, width 0.5 mm, 230 meshes/cm^2) was employed, as shown in Fig. 3(b). The meshes were mechanically compressed within the ceramic housing with a load of 400 g/cm^2 to ensure homogeneous current distribution across the 81 cm^2 active area. Both meshes were spot-welded to platinum wires, which served as external current leads to the power supply system within the high temperature environment. Platinum was selected to provide stable electrical contact and to minimize additional contact resistance during controlled laboratory-scale single-cell testing. While Pt meshes are not representative of industrial stack interconnect systems, their use enables reproducible electrochemical characterization under oxidizing operating conditions.

To enable the operation of single cells under co-electrolysis conditions, a dedicated test rig was utilized, as illustrated in Fig. 3(a). The setup consists primarily of a controlled gas supply system, a custom-built steam generator, several electrical gas heating units, and a chamber furnace. The mixing of the inlet gases is managed through the gas supply system, in which the respective mass flow controllers regulate the flow rates, while steam is supplied independently via a dedicated steam generator. The evaporator is supplied with deionized water by a dosing pump, and the steam produced is regulated by a pneumatic needle valve. Multiple electrical pre-heaters are employed in order to guarantee a precise gas temperature within the pipes of the fuel feed, thus preventing the condensation of steam. The first electrical pre-heater raises the temperature of the dry gas mixture to approximately 200 °C before steam is introduced to the fuel stream. The generated steam is maintained at the same temperature by a trace heating system. The second pre-heater ensures that the humidified gas mixture reaches the SOEC furnace at a suitable temperature of approximately 500 °C, preventing excessive cooling of the single cell upon entry. After exiting the furnace, the fuel outlet gases pass through an air-cooled condenser to capture condensable species. This prevents condensation along the lines leading to the gas analysis system, thereby protecting measurement cells and the exhaust infrastructure from damage. All off-gases are fed into the institute's chimney infrastructure. There a post-combustion stage oxidizes any toxic CO prior to atmospheric release. Furthermore, the experimental setup included a control unit (not shown), a dedicated power supply, an impedance measurement system (galvanostat), and a gas analyzer to measure the inlet and outlet of the SOEC fuel stream. This enabled comprehensive in-operando characterization of the cell performance. The SOEC furnace incorporates a custom-designed ceramic housing for single-cell testing, developed in-house and previously described in our earlier works from our research group [32–35]. Further information on the experimental configuration utilized in this study can be found in [31], where a comparable setup is described in depth.

2.2. Operating parameters

In this work, two different fuel gas compositions for a specific syngas application within a Power-to-X pathway were tested on two individual SOECs to assess their impact on long-term cell degradation. The

Table 1
Gas inlet compositions of co-electrolysis for different syngas applications.

Comp.	Cell No	SOEC temperature	Inlet concentration fuel			$\dot{V}_{Fuel}$ [a]	$\dot{V}_{Air}$ [b]	P/E [c]	S/C [d]	H_2/CO [e] targeted	H_2/CO [e] measured
			H_2	H_2O	CO_2						
		°C	vol%	vol%	vol%	slpm	slpm	–	–	–	–
MeOH/FT (I, II)	1	800	10	52.2	37.8	1.1	0.55	1/9	1.38	≥2	2.07
CH4 (III)	2	800	10	61.7	28.3	1.1	1.1	1/9	2.18	≥3	3.05

[a] Total volume flow rate at the fuel side.
[b] Total volume flow rate at the air side (air - 21% O_2 in N_2).
[c] Product-to-educt ratio at the fuel inlet.
[d] Steam-to-carbon (= H_2O-to-CO_2) ratio at the fuel inlet.
[e] H_2-to-CO ratio at the fuel outlet.

co-electrolysis gas mixtures were varied in their H_2O/CO_2-ratio, as summarized in Table 1. Each cell was operated in galvanostatic mode at a constant current density of 750 mA/cm^2, corresponding to 50% above the manufacturer's recommended limit for steam electrolysis (Elcogen), to accelerate potential degradation effects under high-load conditions. The total fuel inlet flow rate was fixed at 1.1 slpm, ensuring a reactant utilization below 50% (42.78%). This operational limit was chosen to minimize degradation caused by fuel starvation and to ensure adequate reactant distribution across the active cell area. Under galvanostatic operation, the electrochemical conversion rate of H_2O and CO_2 is directly determined by the applied current density according to Faraday's law. Therefore, for fixed inlet gas composition and total fuel flow rate, the total electrochemical conversion remains constant over time as long as the current is maintained. In addition, a hydrogen concentration of 10vol% was included in all gas mixtures to reduce the risk of Ni reoxidation at the fuel electrode. The inlet gas compositions were chosen to emulate realistic syngas production conditions within a Power-to-X pathway. For the MeOH/FT case, a H_2/CO ratio of ≥2 at the fuel outlet was targeted, whereas for the CH4-based composition a ratio of ≥3 was required. Due to the endothermic nature of the co-electrolysis reactions, all tests were conducted at an operating temperature of 800 °C. To further study the effect of air supply in electrolysis on degradation behavior, the air inlet flow rate was systematically adjusted. For the MeOH/FT mixture, the air flow was set to half the rate used in the CH4 case to reflect the expected industrial operating conditions.

2.3. Experimental procedure & in-operando analysis methods

Prior to initiating the experiments, the cell was assembled into the test setup, and the furnace temperature was gradually increased at a ramp of 1K/min to 800 °C. During this heating stage, the fuel side was purged with nitrogen while air was supplied to the air electrode compartment with a flow rate of 0.05 slpm on both sides. Upon reaching the target temperature, a staged reduction procedure was implemented. Initially, a gas mixture containing 5 vol% H_2 and 95 vol% N_2 was applied for 2 hours. Subsequently, the hydrogen concentration was increased step-wise in increments of 10 vol%, with each step maintained until a stable OCV was observed (OCV variation smaller than ± 5 mV/3 h). This gradual increase continued until full reduction with 100 vol% H_2 was achieved. Following this process, the required operating gas compositions were set using the mass flow controllers or the steam generator's dosing pump. During cell operation, temperature, voltage, current, and gas composition data were continuously monitored and recorded at a frequency of 0.33 Hz. For real-time gas analysis (GA), an ABB [36] instrument was utilized to determine the in-operando gas composition. The GA system was composed of two EL3020 modules and a cooled gas supply line. To prevent condensate accumulation inside the analysis setup, the cooling module was maintained at 5 °C, allowing condensation to be separated before reaching the gas sensor chambers. One of the EL3020 was configured with Uras26 and Caldos27 sensor modules, while the other incorporated a Magnos28 module. The Uras26 module, based on non-dispersive infrared spectroscopy, was used to quantify carbon-containing gases such as CO and CO_2. Hydrogen content (H_2) was measured with the thermal conductivity detector in the Caldos27, whereas oxygen levels (O_2) were determined via the paramagnetic sensing principle of the Magnos28 module. A detailed description of these measurement techniques can be found in Ref. [37].

Table 2
Settings of galvanostatic EIS and corresponding DRT for long-term experiments.

EIS:				
DC mA/cm^2	AC %DC	Frequency range Hz	points per decade	Meas. interval h
750	4	$2 \cdot 10^{-2} \ldots 10^{5}$	>50	2
DRT:				
Regularization λ		Shape factor	f_{min} mHz	f_{max} kHz
5.87		3.41	450 (MeOH/FT) 250 (CH4)	$f@-Z''=0$ (= no L)

To monitor the electrochemical behavior and overall performance of the cell, Electrochemical Impedance Spectroscopy (EIS) was conducted using a galvanostat, paired with a power supply from ©ITECH Electronic CO. LTD. (IT6512C) [38] to supply currents up to 100 A for electrolysis. The EIS experiments were carried out in galvanostatic mode, applying an AC amplitude of 4% of the DC operating current. The EIS measurement methodology followed the fast EIS measurement approach, a concept introduced in Ref. [39], which addresses the limitations of traditional EIS by employing broadband excitation in combination with advanced signal processing methods [40]. The impedance data was then processed to determine the distribution of relaxation times (DRT), offering deeper insight into the underlying electrochemical processes, as previously outlined in the literature [41]. The experimental parameters for EIS and the settings for DRT calculations are summarized in Table 2. During the experiments, any change in current was carried out by the power supply at a constant linear rate of 10 A/min.

2.4. DRT peak interpretation supported by literature

This section presents a comprehensive literature survey to support the interpretation of observed processes and mechanisms in the DRT spectra. Table 3 provides an overview of the typical frequency ranges associated with specific electrochemical processes, facilitating the assignment of peaks in the DRT plots. Processes within the frequency range of 10^2-10^3 Hz were excluded from analysis, as they were not observed in the DRT spectra obtained in this study. All processes are grouped into three frequency ranges according to observed peaks in this study, following a categorization approach commonly adopted in SOC DRT analyses reported in the literature [31,42–44]:

Table 3
Overview of DRT peak positions and their associated electrochemical processes based on literature sources.

Peak	Frequency range		Possible mechanism
P_{LF}	10^0-10^1 Hz	~4	a. Gas diffusion at FE[a] [45]
		~7	b. CO_2 reduction processes [47]
		1–10	c. CO_2/CO conversion at FE [48]
		1–10	d. Gas diffusion at FE [46]
		~10	e. Gas diffusion at AE[b] [50]
P_{MHF}	10^2-10^3 Hz	~100	a. Mass transfer (oxygen surface exchange and diffusion) at AE [50]
		~200	b. Oxygen surface exchange at AE [47]
		200–800	c. Oxygen evolution at the active sites of the AE [49]
		~600, ~1000	d. Charge transfer at AE & FE [45,50]
		~900	e. Charge transfer at AE [47]
		~1000	f. Charge transfer at FE [52]
P_{HF}	10^3-10^4 Hz	~2300	a. Ionic transport through YSZ electrolyte and surface exchange at AE [45]
		2000–8000	b. Charge transfer and mass transfer at FE [49]
		3000–5000	c. Hydrogen evolution at FE [51]
		~6000	d. Charge transfer at FE [47]
		7000–10000	e. Oxide ion and charge transfer at FE [52]

[a] Fuel electrode.
[b] Air electrode.

- P_{LF} (10^0-10^1 Hz): most commonly associated with gas diffusion FE [45,46] and CO_2 reduction [47,48]
- P_{MHF} (10^2-10^3 Hz): typically linked to oxygen evolution [47,49] and charge transfer AE [45,47,50]
- P_{HF} (10^3-10^4 Hz): frequently reported to relate to hydrogen evolution [51] and charge transfer FE [47,49,52]

It should be noted that the assignment of DRT peaks to specific electrochemical processes is based on frequency ranges most commonly reported in the literature and may involve overlapping contributions from multiple mechanisms. The interpretation of individual peaks is therefore inherently non-unique, as several electrochemical and transport phenomena may occur within similar frequency domains. For Ni-YSZ-supported SOECs, the number of resolved DRT peaks depends strongly on the selected frequency window and regularization parameters and is further influenced by temperature, current density, and gas composition. Under the present co-electrolysis conditions (800 °C, 750 mA/cm^2) and within the analyzed frequency range (1 Hz–10 kHz), three dominant DRT regions were reproducibly resolved. Comparable studies conducted under similar temperature ranges and frequency windows likewise report three principal DRT regions (e.g., for cells with Ni-YSZ fuel electrode, Wolf et al. [18], Unachukwu et al. [29], Orlić et al. [53], Graves et al. [54], Königshofer et al. [55] (on stack level)), indicating that peak merging under high-temperature co-electrolysis conditions is common. Each region may therefore comprise contributions from more than one elementary step rather than representing a single isolated mechanism. In the present work, the grouping into P_{LF}, P_{MHF}, and P_{HF} regions primarily serves to enable consistent visualization and comparative evaluation of relative peak evolution during different operating phases rather than strict mechanistic separation. Consequently, the discussed peak assignments represent the most likely dominant contributions inferred from the combined analysis of impedance evolution, operating conditions, and post-mortem microstructural observations.

2.5. Post-test characterization

In order to supplement the results and discussion, a post-test analysis of the electrolysis cells was conducted following long-term operation to assess the degradation mechanisms involved. Additionally, a reduced and commissioned single cell from the same manufacturing batch was examined to provide a reference for the initial microstructure before exposure to extended testing. Microstructural and compositional analyses of selected regions were carried out using a Zeiss Ultra 55 scanning electron microscope (SEM) equipped with an EDAX Super Octane EDXS System detector for energy-dispersive X-ray spectroscopy (EDX). In addition to SEM and EDX analyses, correlative SEM-Raman measurements were performed using a Zeiss Sigma 300 VP scanning electron microscope coupled with a WITec RISE Raman microscope. Raman spectra were acquired with a 532 nm laser (10 mW), using a 100× objective lens (NA = 0.75) and an integration time of 10s. Cross-sectional samples were prepared via Broad Ion Beam (BIB) polishing for detailed examination. Porosity was determined using ImageJ2 software [56,57], following common practice in SOC microstructural analysis [58]. The images were binarized using a consistent global thresholding procedure applied identically to all samples to distinguish pore space from solid phases. The pore fraction was calculated as the area percentage of void regions relative to the total analyzed layer area. The reported values therefore represent 2D area fractions suitable for comparative evaluation between samples.

3. Results and discussion

The subsequent sections present the results obtained from the single-cell long-term investigations. For both syngas application cases the long-term operating behavior and therefore the suitability for real applications within Power-to-X paths are shown. Furthermore, a detailed investigation of electrolysis processes and associated losses is carried out using electrochemical impedance spectroscopy combined with DRT calculations, supported by a post-mortem analysis.

3.1. Initial cell performance

Fig. 4 presents the initial performance from both cells operated under co-electrolysis conditions, one with Comp. MeOH/FT and one with Comp. CH4 at 800 °C. Measurements were carried out using a current ramp of 10 A/min up to a maximum current density of 750 mA/cm^2. The polarization curve data collected was subsequently smoothed with a Savitzky-Golay filter to facilitate clearer comparisons at lower current densities. The filter was applied with a window length of 51 points (equivalent to 3% of the dataset size) and a polynomial order of 1. The filtering process was implemented in Python using the Scipy package, based on established methods described in the literature [59,60]. The open-circuit voltage (OCV) measured for both compositions was 0.833 V, which agrees well with the calculated Nernst potentials ($E_{N,MeOH/FT} = 0.841\ V$ and $E_{N,CH4} = 0.840\ V$). These values were obtained using the Cantera package in Python according to Eq. (5) [9,61]

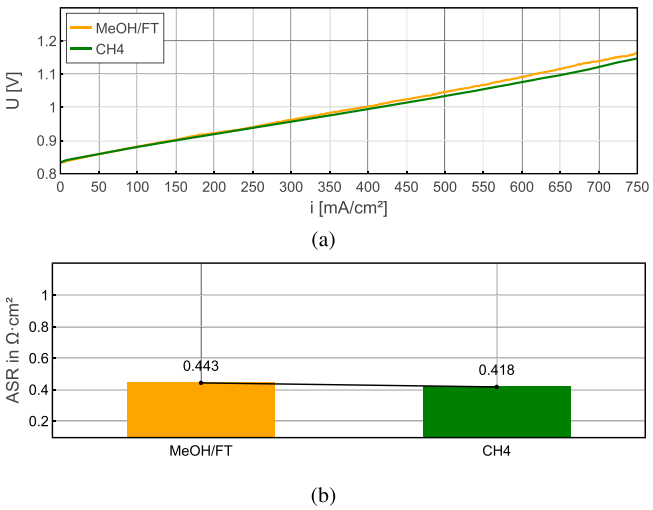

Fig. 4. Comparison of initial cell performance under both operating conditions: (a) polarization curves, and (b) ASR of Comp. MeOH/FT- and Comp. CH4.

with $p_{O_2} = 0.21$ (air). The input compositions for Comp. MeOH/FT and Comp. CH4 were determined from thermodynamic equilibrium calculations at 800 °C using HSC Chemistry 10 [62], accounting for changes due to the RWGS reaction (see Eq. (3)). At 800°C, OCV values below 1V are expected because the reversible potential ΔG/(2F) decreases with temperature and the Nernst term depends on the actual gas ratios (e.g., p_{H_2}/p_{H_2O}) in the inlet with higher product content. The RWGS-adjusted equilibrium composition further affects the CO/CO_2 contribution in co-electrolysis. The used partial pressures and Gibbs free energy ΔG can be found in Appendix A in Tab. A1. At a current density of 750 mA/cm^2, the measured potential decreases with a higher substitution of CO_2 by H_2O, reaching 1.167 V for co-electrolysis with Comp. MeOH/FT and, in co-electrolysis with Comp. CH4 1.142 V. Literature [9,63] suggests that concentration losses are typically more pronounced during CO_2-electrolysis reactions compared to H_2O-electrolysis, which results in increased over-potentials with higher CO_2-contents. A comparable trend was reported in our previous study [31], which examined the short-term effects of CO_2 and H_2O on cell performance.

$$E_N = -\frac{\Delta G_{H_2O}(T)}{2F} - \frac{RT}{2F}\ln\left(\frac{p_{H_2}\cdot p_{O_2}^{1/2}}{p_{H_2O}}\right) = -\frac{\Delta G_{CO_2}(T)}{2F} - \frac{RT}{2F}\ln\left(\frac{p_{CO}\cdot p_{O_2}^{1/2}}{p_{CO_2}}\right) \quad (5)$$

In order to facilitate a comparison of performance across different gas compositions, the area-specific resistance (ASR) was utilized in accordance with the approach that has been commonly reported in the extant literature [16,64,65]. The ASR can be expressed as shown in Eq. (6).

$$ASR = \frac{U_{op} - U_{OCV}}{i_{op}} \quad (6)$$

where U_{op} denotes the potential at the applied operating current i_{op} and U_{OCV} represents the open-circuit voltage. Fig. 4(b) shows the ASR values for Comps. MeOH/FT and CH4. In co-electrolysis, the ASR for syngas application in methanation (CH4) is 0.418 Ωcm^2, slightly lower than that for methanol or FT synthesis (MeOH/FT) at 0.443 Ωcm^2, consistent with the corresponding polarization curves.

3.2. Long-term stability of SOEC for MeOH/FT-case

The long-term stability test for the MeOH/FT-case was performed under 60.75 A (750 mA/cm^2) and a temperature of 800 °C, following the initial performance evaluation of the cell. Fig. 5 presents the cell voltage, the corresponding ASR calculated using Eq. (6), the H_2/CO ratio at the cell's outlet measured via GA, and the temperature change relative to the initial value over a 280-hour period.

As shown in Fig. 5(a), no degradation was detected during the first 52 hours (t_1) of operation. Instead, an initial improvement phase was observed, during which the cell voltage decreased from 1.168 V to 1.142 V, corresponding to a reduction of 26 mV (0.5 mV/h) and an improvement of 2.2%. A comparable trend was recorded for the ASR, which declined from 0.447 to 0.413 Ωcm^2, a decrease of 34 mΩcm^2 (0.65 mΩcm^2/h), representing a relative improvement of 7.6%. Following this phase, degradation occurred for the remainder of the long-term stability test. To quantify this, the degradation rates (DR) for voltage and ASR were calculated using Eqs. (7) and (8), respectively, with the results extrapolated to a 1000-hour operating period.

$$DR_U = \frac{U_{t_2} - U_{t_1}}{U_{t_1}} \cdot 100\% \cdot \frac{1000}{t_2 - t_1} \quad (7)$$

$$DR_{ASR} = \frac{ASR_{t_2} - ASR_{t_1}}{ASR_{t_1}} \cdot 100\% \cdot \frac{1000}{t_2 - t_1} \quad (8)$$

where U and ASR represent the voltage and area-specific resistance, respectively, at a given time t during the experiment. During the degradation phase, the voltage rose to 1.158 V, representing an increase of 15.7 mV over 228 h (68.7 mV/1000 h) and corresponding to a DR_U of 6.01%/1000 h. The ASR showed a comparable trend, increasing by 21 mΩcm^2 to 0.434 Ωcm^2 within 228 h, equivalent to 92 mΩcm^2/1000 h and a DR_{ASR} of 22.2%/1000 h. As shown in Fig. 5(b), the H_2/CO ratio remained stable at approximately 2.07 throughout the experiment, resulting from the fixed current density and the corresponding constant outlet gas composition. Although minor temperature variations occurred during degradation due to changes in resistive losses, such variations (≤0.5 K at 800 °C) have only a negligible thermodynamic influence on the temperature-dependent RWGS equilibrium. The experimentally measured outlet composition confirms that the H_2/CO ratio remained stable within the measured range. The two peaks, one at the beginning and another at around 120 h, were attributed to temporary interruptions of the fuel outlet line to the gas analyzer during checks on the GA unit. Fig. 5(c) depicts the temperature variation on both sides of the cell relative to the initial temperature of 800 °C, with each curve representing the mean temperature change measured by six thermocouples on the respective electrode. The near overlap of the two curves indicates comparable temperature behavior at both electrodes. A comparison with the voltage data reveals a clear correlation: during the initial improvement phase, the voltage decrease coincided with a drop in temperature, consistent with reduced resistance and lower heat generation. In contrast, during the degradation phase, the voltage increase was accompanied by a temperature rise, indicative of higher resistive losses.

In order to gain a better understanding of the mechanisms underlying the initial improvement and subsequent degradation, the evolution of impedance and corresponding DRT spectra in each phase is examined in the following section.

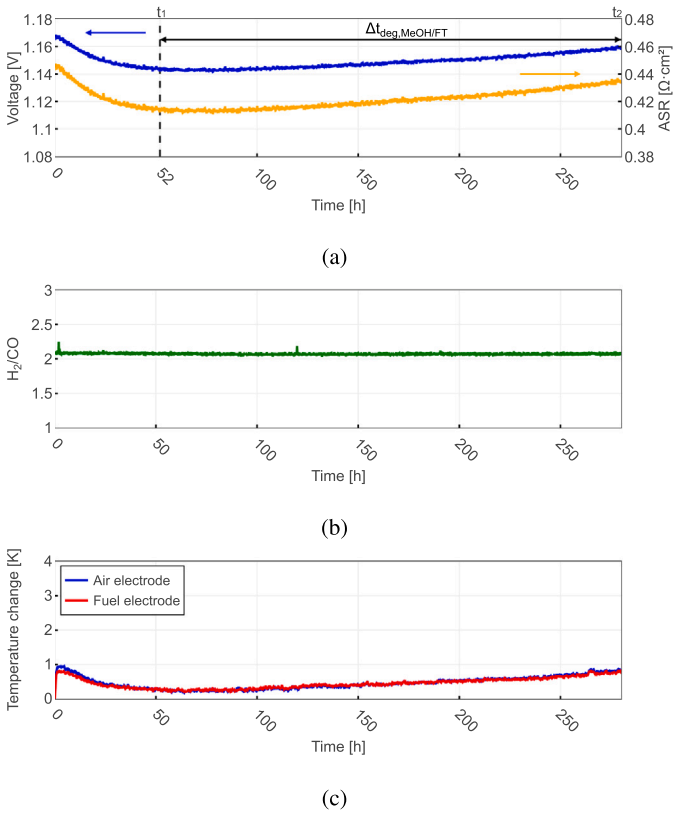

Fig. 5. Recorded monitoring data for the single cell operated with Comp. MeOH/FT at a current density of 750 mA/cm^2: (a) voltage and ASR, (b) H_2/CO-ratio, and (c) shift in temperature at both electrodes relative to the starting state.

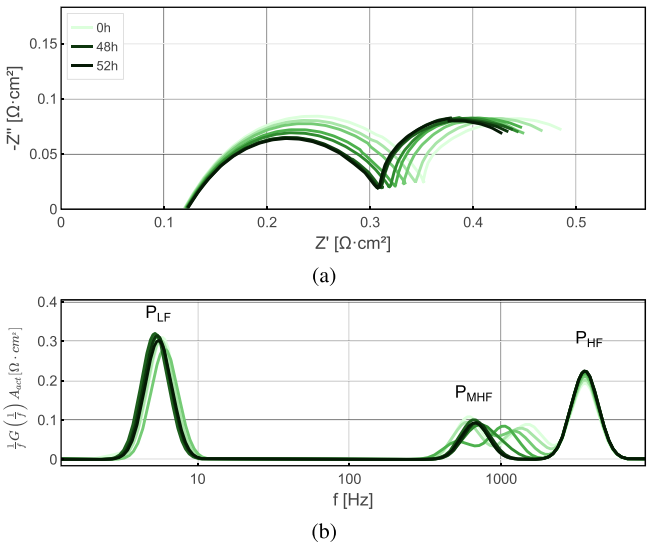

Fig. 6. Electrochemical analysis of the initial improvement phase for the single cell operated with Comp. MeOH/FT at a current density of 750 mA/cm^2. Impedance spectra and corresponding DRT plots are shown at 8-hour intervals from 0 to 48 h, with an additional spectrum at 52 h (t_1, end of phase): (a) Nyquist plots, (b) DRT spectrum.

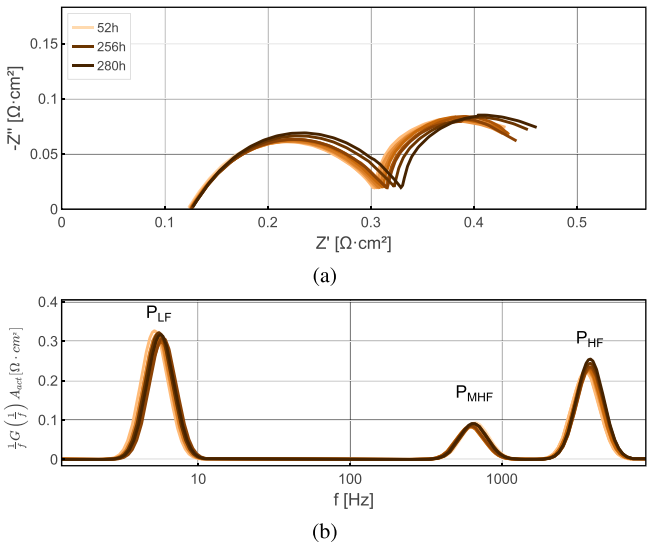

Fig. 7. Electrochemical analysis of the degradation phase for the single cell operated with Comp. MeOH/FT at a current density of 750 mA/cm^2. Impedance spectra and corresponding DRT plots are shown at 24-hour intervals from 52 h (t_1) to 256 h, with an additional spectrum at 280 h (t_2, end of phase): (a) Nyquist plots, (b) DRT spectrum.

3.2.1. Initial improvement phase

Fig. 6 presents the electrochemical analysis of the improvement phase under operation with Comp. MeOH/FT at 750 mA/cm^2. Impedance spectra and the corresponding DRT plots are shown at 8-hour intervals from the start of the long-term stability test up to 48 h, with curves color-coded from light to dark green according to testing duration. Data from the end of the phase at 52 h (t_1) is also included. Throughout the entire phase, the ohmic resistance (R^{Ω}) remained constant at 0.122 Ω · cm^2 (1.5 mΩ), indicating no changes in either the electrical contact resistance or the electrolyte resistance. The latter stability can be attributed to the minimal variation in the mean cell temperature (less than 0.5 K, as can be seen in Fig. 5c) and the thin electrolyte layer of the fuel-electrode-supported cell. The Nyquist plot further shows that co-electrolysis exhibits two distinct arcs, hereafter referred to as the high-frequency arc (left) and the low-frequency arc (right). The EIS spectra indicate that high-frequency losses decreased over the phase, whereas low-frequency losses remained largely unchanged. This is most consistent with an improvement in charge-transfer-related processes, while diffusion-related mechanisms remained stable. Consequently, the overall polarization resistance (R_P) decreased, leading to a reduction in total resistance, which explains the observed voltage trend. A more detailed assessment of changes in R_P is provided by the DRT analysis of the EIS spectra, in which each peak corresponds to a process in either the fuel or air electrode, and the area under each peak represents the magnitude of the resistance associated with that process.

The DRT spectra reveal three to four peaks grouped within two distinct frequency regions: a high-frequency peak (P_{HF}) at approximately 3500 Hz, which is most consistently associated with processes primarily occurring at the Ni-YSZ fuel electrode, including charge-transfer mechanisms and hydrogen evolution that are not fully separated under these operating conditions; mid-high-frequency peaks (P_{MHF}) between 500 and 1100 Hz, most consistently associated with oxygen evolution and surface-exchange-related processes at the air electrode, while overlapping charge-transfer contributions from both electrodes cannot be fully excluded; and a low-frequency peak (P_{LF}) near 5 Hz, most consistent with gas diffusion and CO_2 conversion. These peak regions correspond well to the two arcs observed in the Nyquist plot: the high-frequency arc relates to P_{HF} and P_{MHF}, while the low-frequency arc corresponds to P_{LF}.

During the initial phase, high-frequency losses (P_{HF}) remained nearly constant, whereas losses in the mid-high-frequency region decreased. Specifically, two peaks initially located at 500 and 1100 Hz merged into a single peak at 700 Hz, indicating reduced resistance in the P_{MHF} region. This behavior is most consistent with reduced losses associated with oxygen evolution and charge transfer at the air electrode. Such an improvement in air-electrode kinetics is consistent with the microstructural observations discussed in Section 3.4, where Pt migration from the contacting mesh toward the LSC surface was identified. The presence of Pt at the air-electrode surface enhances oxygen surface exchange and reduces polarization resistance (R_P) of the high-frequency arc observed in the Nyquist plot, thereby explaining the improved impedance response. Losses associated with gas diffusion and CO_2-conversion (P_{LF}) remained largely unchanged, aside from a slight frequency shift (~0.6 Hz), suggesting that no major structural changes in the fuel electrode were dominant within this phase.

3.2.2. Degradation phase

Fig. 7 illustrates the electrochemical characterization of the degradation phase of Comp. MeOH/FT operated at 750 mA/cm^2. Impedance spectra and the corresponding DRT plots were selected at 24-hour intervals between 52 (t_1) and 256 h, with an additional dataset presented at 280 h (t_2), yielding a total degradation period of 228 h. To highlight the temporal evolution of losses, the curves are color-coded from orange (beginning) to dark brown (end of the phase). Similar to the initial improvement phase, two distinct features, a high-frequency arc and a low-frequency arc, are observed in the EIS spectra during degradation (Fig. 7(a). The high-frequency resistance progressively increases, whereas the low-frequency losses remain largely unchanged, suggesting a deterioration of charge-transfer processes while diffusion-related mechanisms are unaffected. Consequently, the total polarization resistance rises over time. The ohmic resistance (R^{Ω}) remains constant at approximately 0.122 Ω · cm^2 (1.5 mΩ), indicating that ohmic losses were unaffected by degradation. This increase in resistance explains the gradual rise in cell voltage in Fig. 5.

The DRT spectra in Fig. 7(b) show that the changes in R_P during degradation were driven by different mechanisms than those observed in the initial improvement phase, which led to a lower resistance. The high-frequency peak (P_{HF}) near 3500 Hz increased slightly and shifted

to around 3700 Hz, whereas it remained unchanged during the improvement phase. This behavior is most consistent with increased charge- and mass-transfer losses at the Ni-YSZ fuel electrode, indicating that fuel-electrode-related contributions likely play a dominant role in the observed resistance increase. The mid-high-frequency peak (P_{MHF}) at ~600 Hz followed a similar trend, showing increased resistance and a small shift to ~640 Hz, which is most consistent with reduced oxygen evolution activity or increased charge-transfer losses at the air electrode. In contrast, the low-frequency peak (P_{LF}) remained essentially stable and just slightly increased near 5 Hz, with peak values between 0.3 $\Omega \cdot cm^2$ (3.7 mΩ) and 0.324 $\Omega \cdot cm^2$ (4.0 mΩ), showing no clear trend over time. To substantiate these findings, SEM and EDX analyses were performed on the tested cell, as presented in Section 3.4.

3.3. Long-term stability of SOEC for CH4-case

The long-term stability assessment for the CH4-case was carried out at 60.75 A (750 mA/cm^2) and 800 °C, following the cell's initial performance test. Fig. 8 displays the cell voltage, the corresponding ASR calculated from Eq. (6), the H_2/CO ratio at the outlet determined by gas analysis, and the temperature deviation from the initial value over a duration of 500 hours. As shown in Fig. 8(a), the second cell operated with Comp. CH4 also exhibited an initial improvement phase. In contrast to Comp. MeOH/FT (Fig. 5a), this period was shorter, lasting only 30 h (t_1). During this phase, the cell voltage decreased from 1.140 to 1.100 V, corresponding to a reduction of 40 mV (1.3 mV/h) and an improvement of 3.5%. The ASR showed a similar trend, declining from 0.409 to 0.356 Ωcm^2, equivalent to 53 mΩcm^2 (1.77 mΩcm^2/h) and a relative improvement of 12.9%. After this initial boost in performance, degradation set in. Using Eqs. (7) and (8), the

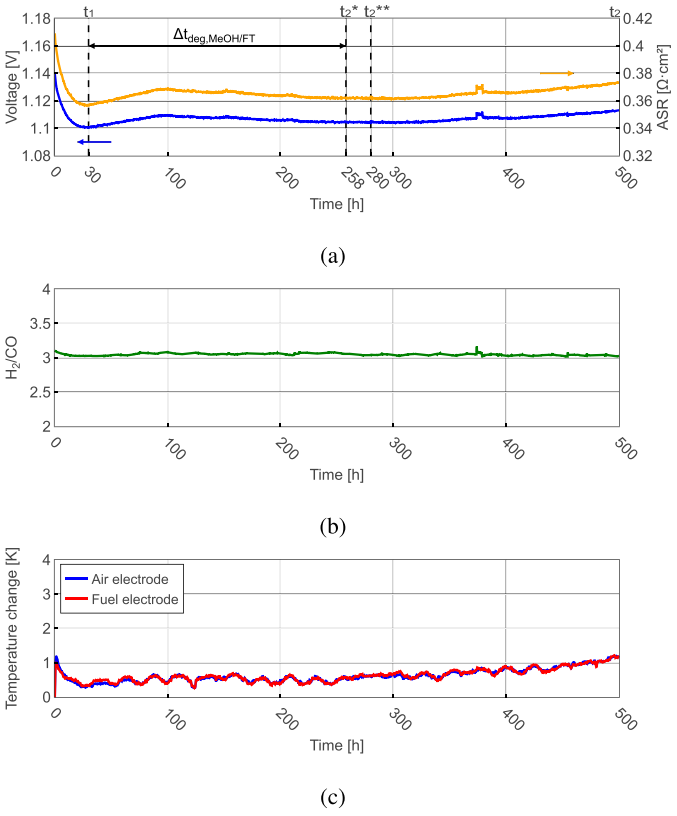

Fig. 8. Recorded monitoring data for the single cell operated with Comp. CH4 at a current density of 750 mA/cm^2: (a) voltage and ASR with vertical dashed lines indicating 258 h (aligned degradation-phase duration with MeOH/FT) and 280 h (aligned total test duration), (b) H_2/CO-ratio, and (c) shift in temperature at both electrodes relative to the starting state.

degradation rates were determined: over 470 h up to t_2 the voltage increased to 1.113 V, corresponding to 12.3 mV (27.3 mV/1000 h) and a DR_U of 2.48%/1000 h. Over the same period, the ASR rose by 17 mΩcm^2 to 0.373 Ωcm^2, corresponding to 36 mΩcm^2/1000 h and a DR_{ASR} of 10.2%/1000 h. To evaluate the potential influence of differing total test durations and possible cumulative time effects on the comparison of degradation rates, the CH4 case was additionally analyzed over truncated time windows aligned with the MeOH/FT experiment. When limited to 30–280 h (t_1-t_2**), corresponding to the same total operating time as the MeOH/FT test, the voltage degradation rate amounts to 16.4 mV/1000 h (1.49%/1000 h), with a corresponding ASR degradation rate of 21.9 mΩcm^2/1000 h (6.15%/1000 h). Furthermore, when evaluated over 30–258 h (t_1-t_2*), which matches the degradation-phase duration of the MeOH/FT case ($\Delta t_{deg,MeOH/FT}$ = 228 h), the voltage and ASR degradation rates are 18.4 mV/1000 h (1.67%/1000 h) and 24.6 mΩcm^2/1000 h (6.88%/1000 h), respectively. Both truncated evaluations yield lower degradation rates than those obtained over the full 30–500 h interval (27.3 mV/1000 h and 36 mΩcm^2/1000 h), indicating a progressive increase in the apparent degradation rate with operating time under CH4 conditions. This observation suggests that cumulative degradation effects become more pronounced beyond approximately 280–300 h. Nevertheless, the qualitative comparison between operating conditions remains unchanged, as the MeOH/FT case exhibits substantially higher degradation within its investigated interval (52-280 h), confirming that the observed differences are not solely attributable to the differing total test durations.

As shown in Fig. 8(b), the H_2/CO ratio remained essentially constant at 3.05 throughout the long-term test. As discussed in Section 3.2, this stability results from the galvanostatic operation mode, which enforces a fixed outlet gas composition due to constant current. Despite small temperature fluctuations observed (≤0.5 K at 800 °C), no recognizable shift in the outlet H_2/CO ratio was detected over time, indicating that the imposed galvanostatic conditions ensured stable syngas production throughout the experiment. Fig. 8(c) depicts the mean temperature evolution of both electrodes. Similar to the first cell, the curves overlap, indicating comparable thermal behavior of the electrodes. A clear correlation between voltage and temperature is evident: when resistive losses decreased, the temperature dropped, and vice versa. Compared with the cell operated under Comp. MeOH/FT conditions (Fig. 5(c), the observed temperature change is slightly higher for Comp. CH4. This difference may be attributed to the less endothermic character of Comp. CH4, which contains a higher H_2O/CO_2 ratio and consequently a reduced CO_2 content (see Eqs. (1)–(3)). To further clarify the mechanisms underlying both phases, the evolution of impedance and the corresponding DRT spectra are examined in the following section.

3.3.1. Initial improvement phase

Fig. 9 presents the electrochemical characterization of the improvement phase for the second cell operated with Comp. CH4 at 750 mA/cm^2. Nyquist plots and the corresponding DRT spectra are shown from the beginning of the long-term test up to 28 h, plotted at 4-hour intervals. In addition, data from the final measurement of the improvement phase at 30 h (t_1) is included. The ohmic resistance (R^{Ω}) remained essentially constant at 0.122 $\Omega \cdot cm^2$ (1.5 mΩ) throughout the phase (Fig. 9a), indicating stable electrolyte and contact resistances. Two distinct arcs are observed in the impedance spectra: a high-frequency arc associated with charge-transfer processes and a low-frequency arc attributed to mass-transport (diffusion) limitations. The temporal evolution of the spectra reveals a pronounced decrease in high-frequency losses compared with the first cell operated under Comp. MeOH/FT conditions, whereas the low-frequency contribution remains largely unchanged. This interpretation is further supported by the DRT analysis shown in Fig. 9(b), which provides deeper insights into charge-transfer-related processes during the improvement phase. As in the DRT spectra obtained for Comp. MeOH/FT, the spectra of the second cell operated with Comp. CH4 (Fig. 9b) initially display four distinct peaks that can

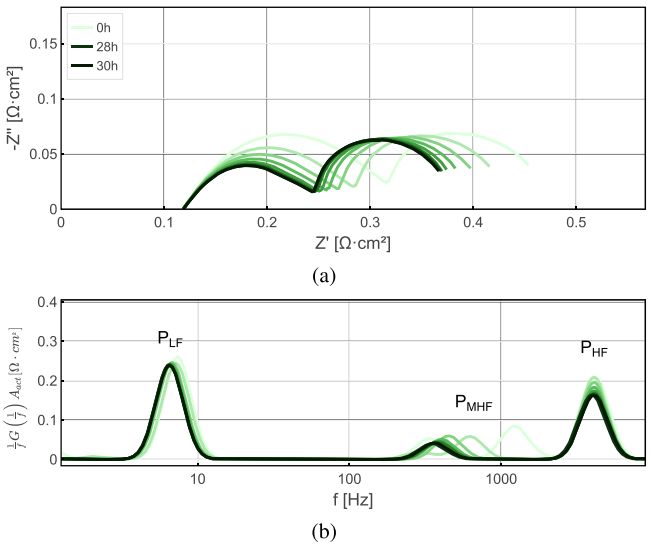

Fig. 9. Electrochemical analysis of the initial improvement phase for the single cell operated with Comp. CH4 at a current density of 750 mA/cm^2. Impedance spectra and corresponding DRT plots are shown at 4-hour intervals from 0 to 28 h, with an additional spectrum at 30 h (t_1, end of phase): (a) Nyquist plots, (b) DRT spectrum.

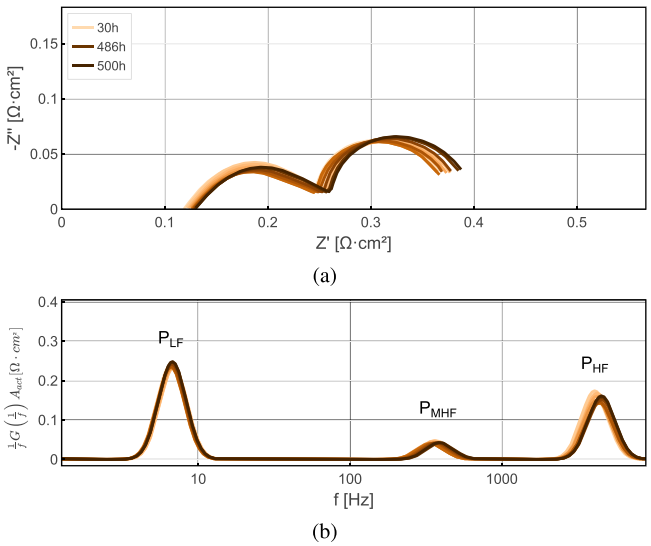

Fig. 10. Electrochemical analysis of the degradation phase for the single cell operated with Comp. CH4 at a current density of 750 mA/cm^2. Impedance spectra and corresponding DRT plots are shown at 48-hour intervals from 30 h (t_1) to 486 h, with an additional spectrum at 500 h (t_2, end of phase): (a) Nyquist plots, (b) DRT spectrum.

be grouped into two frequency regions. A high-frequency peak (P_{HF}) appears around 4 kHz, most consistently associated with fuel-electrode-dominated processes, including charge-transfer and hydrogen evolution at the Ni-YSZ interface. One to two peaks are observed in the mid-high frequency range (P_{MHF}: 340–1200 Hz), which may be attributed to reactions associated with oxygen evolution at the air electrode or charge-transfer. Finally, a low-frequency peak (P_{LF}) emerges at approximately 6.5 Hz, most consistent with gas-phase diffusion and CO_2 conversion phenomena. The evolution of the DRT spectra during the improvement phase revealed that high-frequency losses (P_{HF}) decreased, while mid-high-frequency peaks (P_{MHF}) underwent more pronounced changes. The two initial peaks at 340 and 1200 Hz merged into a single peak shifted to ~370 Hz. The reduction in P_{MHF} losses is most consistent with reduced losses associated with oxygen evolution and charge-transfer processes at the air electrode. This behavior is consistent with the Pt redistribution toward the LSC surface identified in Section 3.4, where Pt incorporation enhances oxygen electrode activity and reduces polarization resistance. These changes in P_{HF} and P_{MHF} correspond to the reduction of the high-frequency arc observed in the impedance spectra. In contrast, the low-frequency peak P_{LF}) at 6.5 Hz remained largely stable. Only a slight decrease in resistance was observed between the first and second spectra, followed by a minor downward shift of ~1 Hz in the subsequent measurements, suggesting limited changes in gas-diffusion and CO_2-conversion related losses.

3.3.2. Degradation phase

Fig. 10 shows the EIS of the degradation phase of Comp. CH4 operated at 750 mA/cm^2 for a total of 470 h. For clarity, impedance spectra and the corresponding DRT plots are displayed at 48-hour intervals from 30 (t_1) to 486 h, with an additional measurement outside the interval pattern at 500 h (t_2). The curves are color-coded from light orange at the beginning of the phase to dark brown at its end to illustrate the temporal evolution of losses. As observed for Comp. MeOH/FT, two characteristic arcs, a high-frequency and a low-frequency arc, are visible in the Nyquist plot of Comp. CH4 (Fig. 10a). During the degradation phase, the high-frequency contribution increased after 500 h, while the low-frequency seemed to remain nearly unchanged. This points to a progressive deterioration of charge-transfer losses, whereas diffusion-related mechanisms seem largely unaffected. As a result, the overall polarization resistance rose with time. In addition, the ohmic resistance (R^{Ω}) showed a slight increase from 0.122 Ω · cm^2 (1.5 mΩ) to 0.130 Ω · cm^2 (1.6 mΩ), suggesting a minor contribution of ohmic degradation [66]. The slight increase in R^{Ω} is most plausibly associated with a moderate increase in contact resistance at the fuel electrode. While interfacial degradation between YSZ and Ni-YSZ has been reported to contribute to ohmic growth under certain conditions (e.g., Tao et al. [17]), no clear signs of interfacial deterioration were observed in the post-mortem SEM analysis (see Section 3.4). Instead, Ni agglomeration and surface roughening were identified in the contact layer, which likely reduced the effective electrical contact area and thereby contributed to the gradual increase in ohmic resistance.

The corresponding DRT spectra (Fig. 10b) demonstrate that the mechanisms governing resistance changes during degradation differ from those in the initial improvement phase. The high-frequency peak (P_{HF}), located near 4 kHz, initially decreased in magnitude until the measurement at 318 h, before increasing again toward 500 h. In addition, the peak shifted slightly to ~4.4 kHz. This behavior suggests an initial improvement followed by a deterioration, most likely related to changes in dominant fuel-electrode-associated contributions, including charge-transfer and mass-transport processes. The mid-high-frequency peak (P_{MHF}) around 370 Hz remained stable in magnitude but shifted slightly to ~380 Hz, suggesting that oxygen evolution activity was likely not the dominant contributor to the observed resistance change. In contrast, the low-frequency peak (P_{LF}) near 6.5 Hz increased modestly, most consistent with increased losses associated with diffusion and/or CO_2-conversion processes. Overall, the degradation phase is characterized by a gradual rise in R^{Ω}, a slight increase in diffusion- and CO_2-related losses, stable resistance contributions from oxygen evolution and charge transfer in the mid-high frequencies, and a high-frequency peak (P_{HF}) that decreased until 316 h before increasing again. These combined effects account for the voltage trend observed in Fig. 8(a), where an initial rise is followed by a decrease up to ~316 h, and then a subsequent increase driven by the evolution of P_{HF}. To further support these findings, post-test SEM and EDX analyses were carried out, as presented in Section 3.4.

3.4. Post mortem analysis

As part of the post-mortem analysis, SEM investigations were conducted along the cell centerline in the flow direction, focusing on

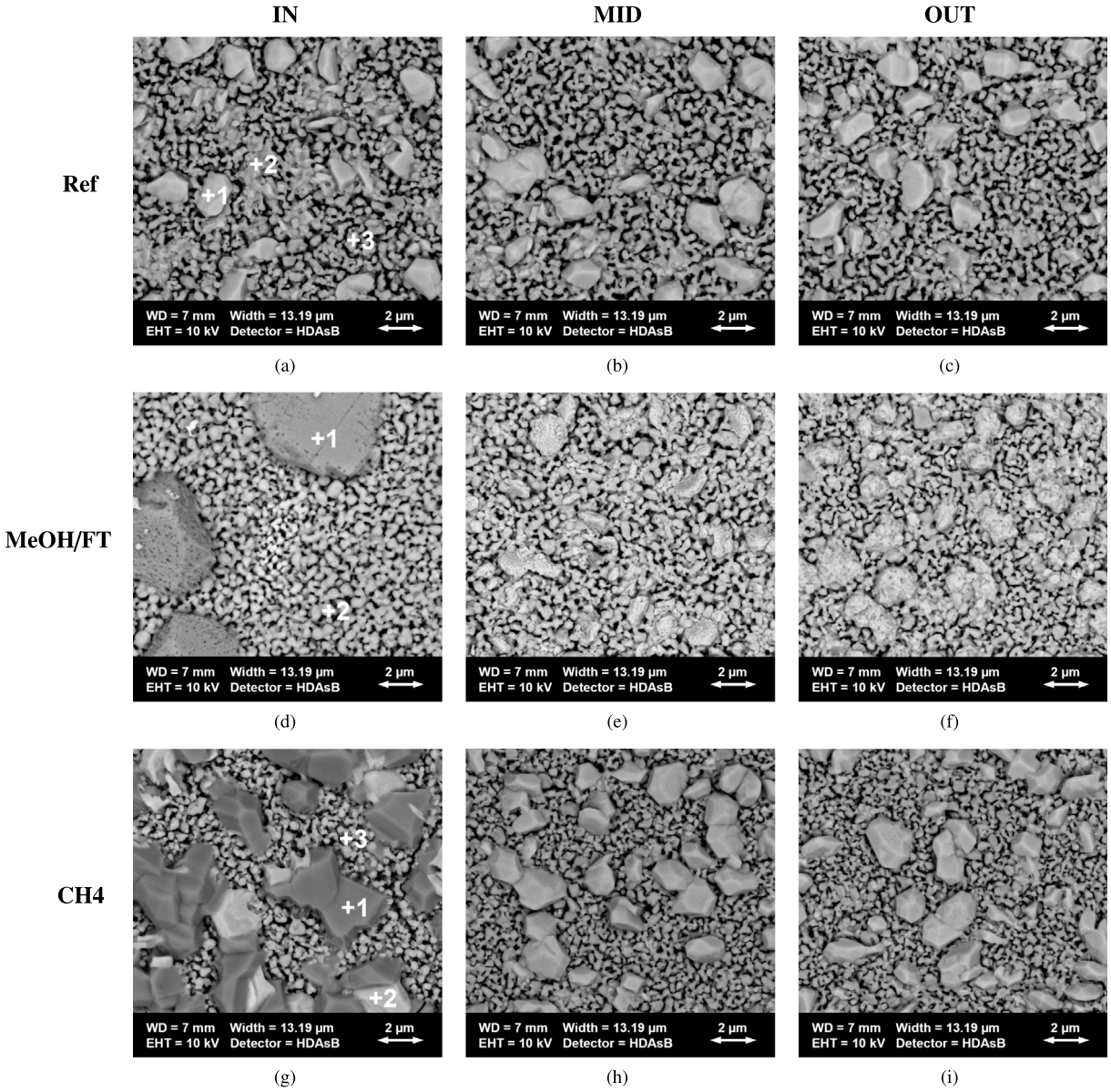

Fig. 11. SEM surface images of the air electrode of all cells (WD-Working Distance, EHT-Electron High Tension): (a) initial state IN, (b) initial state MID, (c) initial state OUT, (d) MeOH/FT IN, (e) MeOH/FT MID, (f) MeOH/FT OUT, (g) CH4 IN, (h) CH4 MID, and (i) CH4 OUT.

the inlet (IN), middle (MID), and outlet (OUT) regions of both tested cells, as well as on an additional reduced cell (Ref) used as a reference for the initial state. Both the substrate surface and cross sections were examined to assess microstructural changes induced during long-term operation. In addition, EDX analyses were performed to detect potential changes in material composition. These combined analyses provided detailed insights into the cell's initial architecture and its evolution under specific operating environments (Comp. MeOH/FT and Comp. CH4).

Air electrode surface

SEM images of the air electrode are shown in Fig. 11. The reference cell, presented in Fig. 11(a)–(c), displays the surface morphology of the air electrode in its state prior to long-term testing, revealing the grain structure of $La_{1-x}Sr_xCoO_{3-\delta}$ (LSC). After reduction and subsequent cell commissioning under steam electrolysis conditions at 800 °C, multiple grain sizes and distinct phases were observed across all positions. Smaller LSC grains (3 in Fig. 11a) likely represent the original microstructure, while larger Sr-rich grains with reduced Co content (1) are indicative of phase segregation. Platinum was detected within these larger grains, suggesting diffusion from the Pt contact mesh. The Pt current collector was the only Pt-containing component, supporting this assignment. It should be noted that in practical stack configurations, metallic interconnect systems are typically used instead of Pt meshes. Therefore, the observed Pt migration represents a contacting-specific effect associated with the experimental configuration rather than an inherent limitation of the cell design under industrial operation. Transitional regions (2) between the small and large grains exhibit intermediate Sr and Co concentrations. This microstructure was defined as the reference state, since all cells underwent identical reduction and commissioning procedures. The corresponding porosities determined at the IN, MID, and OUT positions ranged from 15.5 to 17.5%, as summarized in Table 4. The corresponding EDX point data can be found in Appendix A.

For Comp. MeOH/FT, pronounced structural changes were observed on the air-electrode surface after 280 h of operation (Fig. 11(d)–(f)). At the inlet (IN) in Fig. 11(d), large Sr- (1) and Pt-rich grains formed

Table 4
Calculated porosities (in %) derived from SEM surface images of the air electrode acquired at a magnification five times lower than that used in Fig. 11.

Pos	IN	MID	OUT
Ref	16.5	17.5	15.5
MeOH/FT	11.1	9.9	8.7
CH4	9.5	14.3	12.9

within the original structure (2), whereas smaller grains were found in the MID and OUT regions. This morphological evolution resulted in a notably higher porosity at the inlet, as summarized in Table 4. The overall porosity, however, decreased substantially compared with the initial state, reaching 11.1% at the inlet and almost half of the original values at the MID (9.9%) and OUT (8.7%) positions. It should be noted that the SEM image at the inlet was taken approximately 10 mm toward the cell center (in comparison to the other cells), due to partial delamination of the electrode at the inlet area. When these results are compared with those obtained for Comp. CH4, which was operated for nearly twice the duration of Comp. MeOH/FT, the pronounced porosity reduction may be attributed to the considerably lower air flow rate (0.55 slpm) during operation, resulting in less convective cooling and a higher partial pressure of O_2. Such reduced porosity is likely to hinder oxygen transport through the electrode, limiting the surface exchange and charge-transfer processes. This effect is consistent with the slightly increased losses and the enhanced DRT peak (P_{MHF}) observed in Fig. 7(b). It has to be noted that the simultaneous differences in operating time and fuel composition, however, mean that the independent contribution of air flow cannot be strictly isolated, although the observed microstructural and electrochemical trends remain consistent with such an influence. In the case of Comp. CH4, after 500 h of operation, a comparable microstructural pattern was observed (Fig. 11(g)–(i)). At the inlet (IN) in Fig. 11(g), two distinct grain phases were identified: a Sr-rich phase (1) and a Sr/Pt-rich phase (2) embedded within the original matrix (3). In contrast, only Sr/Pt-rich grains were present in the MID and OUT regions, resulting in a slightly lower porosity at the inlet compared with Comp. MeOH/FT. The grains in Comp. CH4 appeared more developed, consistent with the longer operating duration. The measured porosities at the MID (14.3%) and OUT (12.9%) positions showed minimal deviation from the reference cell, whereas the inlet exhibited a more pronounced reduction (9.5%). These comparatively smaller variations indicate that oxygen transport limitations were less pronounced than in Comp. MeOH/FT, consistent with the absence of pronounced changes in the air-electrode-related losses (P_{MHF}) observed in Fig. 10(b). It should be emphasized that the formation of Sr-rich and Sr/Pt-rich surface regions was observed under both compositions and represents a surface evolution pathway during electrolysis operation. The primary difference between Comp. MeOH/FT and Comp. CH4 lies in the extent of porosity reduction and its electrochemical impact, which are influenced by operating parameters such as air-flow rate, the resulting local oxygen partial pressure, and the test duration, rather than in fundamentally different degradation mechanisms.

As discussed in Sections 3.2.1 and 3.3.1, both cells exhibited an initial improvement phase, characterized by a decrease in the DRT peak associated with charge transfer and the oxygen evolution reaction at the air electrode. This improvement is consistent with Pt diffusion toward the air electrode, where Pt enhances the oxygen surface exchange kinetics, as also reported in previous studies [67–69]. Simner et al. [70] observed a similar phenomenon in a fuel cell (SOFC) configuration, where Pt migration from a current collector improved the activity of an LSF electrode.

In parallel to this initial improvement, Sr surface segregation is expected under electrolysis conditions. The primary driving factors for Sr segregation in LSC-type materials are elevated temperature, high oxygen chemical potential, and anodic polarization. Under anodic polarization in electrolysis (in this study at 750 mA/cm^2, 1.1-1.14 V), oxygen vacancy depletion is enhanced [71], which promotes Sr diffusion toward the surface. At the operating temperature of approximately 800 °C, the thermodynamic tendency for SrO surface segregation is further intensified. Elevated temperature has repeatedly been shown to accelerate Sr segregation in Sr-containing perovskites. For example, Oh et al. [72] reported increased SrO segregation in LSCF between 600 and 900 °C, while Chen et al. [73] and Mutoro et al. [74] demonstrated enhanced Sr-rich phase formation with increasing annealing temperature. Taken together, these findings suggest that the observed Sr enrichment on the air-electrode surface in the present study is consistent with thermally and electrochemically driven segregation mechanisms. In addition to temperature and polarization effects, elevated oxygen partial pressure has been reported to intensify Sr segregation in perovskite oxides [75,76], as increased oxygen chemical potential may enhance the thermodynamic tendency for surface Sr enrichment through modified defect equilibria. In the case of Comp. MeOH/FT, the lower air flow rate (0.55 slpm), and thus reduced convective removal of oxygen, is expected to result in higher local oxygen partial pressure under load compared with Comp. CH4 (1.1 slpm). This condition may have contributed to the formation of larger Sr-rich grains and more pronounced surface segregation at the air electrode. The increased SrO formation at the inlet may further explain the partial delamination observed in this region and the presence of coarser grains after roughly half the operating time. Overall, the observations are consistent with a combined influence of elevated temperature, anodic polarization, and locally increased oxygen partial pressure, which together may accelerate air-electrode degradation through enhanced Sr segregation and surface instability.

Fuel electrode surface

SEM images of the fuel electrode are shown in Fig. 12. The reference cell, presented in Fig. 12(a)–(c), depicts the surface morphology of the fuel electrode in its initial state prior to long-term operation, revealing a Ni contact layer (1) over the grain structure of the Ni-YSZ cermet (3, nickel-yttria-stabilized zirconia). Deposits located at grain boundaries (2), containing Al, Na, Mg, Mn, and Si, are also visible. The corresponding EDX point data can be found in Appendix A. These are most likely residues from the manufacturing process, as similar features were observed on an as-received Elcogen AS cell (see Fig. A.2 in Appendix A). Owing to the presence of the dense contact layer, the porosity obtained from the surface image is considerably lower than that of the air electrode. For the reference cell, the calculated porosity ranges between 5.5 and 5.7%, as summarized in Table 5. It should be noted that these values depend strongly on the selected area in a specific region (IN, MID, or OUT) due to local variations in the contact layer and therefore serve only as an order-of-magnitude estimate.

For the cell operated with Comp. MeOH/FT, no significant structural changes were observed after 280 h of operation (Fig. 12(d)–(f)). The contact layer (1) above the Ni-YSZ structure (2) appears largely unaffected, and fewer deposits are visible along the grain boundaries, suggesting that these residues may have been removed during operation. The measured porosity decreased slightly, ranging from 3.4 to 5%. In the case of Comp. CH4, after 500 h of operation, the grain surfaces of the Ni contact layer (1) appear roughened (Fig. 12(g)–(h)). The combination of increased porosity (5.8-8.8%) and roughened Ni surfaces is consistent with Ni coarsening/agglomeration in the contact layer, which would reduce the effective contact area. Deposits (2) were again visible at the inlet, although fewer were detected overall compared to Comp. MeOH/FT. The reduction in the effective Ni contact area due to agglomeration and the formation of voids could explain the increase in ohmic resistance (R^{Ω}, high-frequency intercept) observed in Fig. 10(a), due to a drop in active surface area. Both cells tested under long-term operation exhibit a similar trend: porosity decreases from the inlet toward the outlet, which may be related to non-uniform local electrochemical activity (likely higher near the inlet). No additional carbon-rich phases were observed in SEM

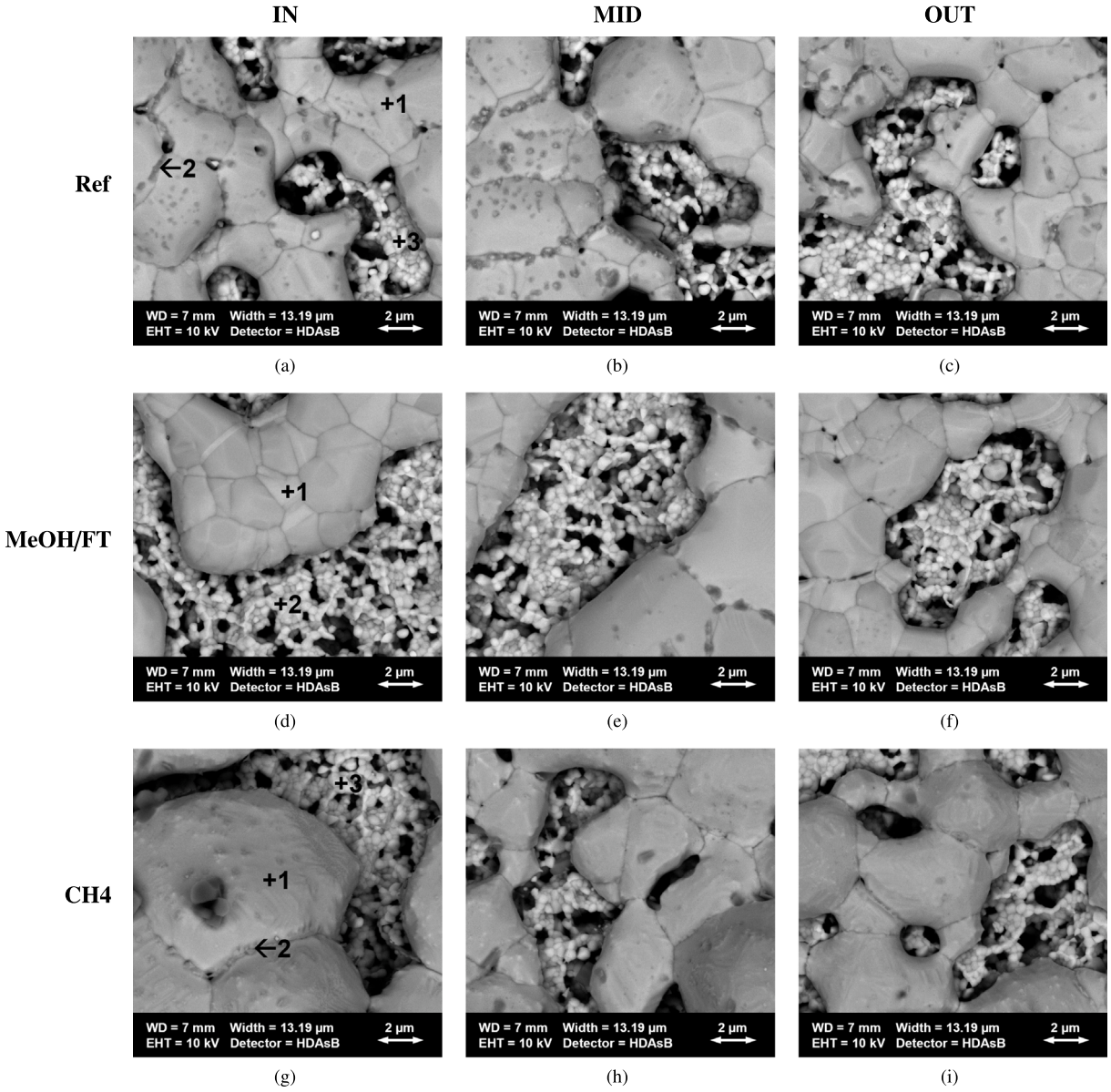

Fig. 12. SEM surface images of the fuel electrode of all cells (WD-Working Distance, EHT-Electron High Tension): (a) initial state IN, (b) initial state MID, (c) initial state OUT, (d) MeOH/FT IN, (e) MeOH/FT MID, (f) MeOH/FT OUT, (g) CH4 IN, (h) CH4 MID, and (i) CH4 OUT.

Table 5
Calculated porosities (in %) derived from SEM surface images of the fuel electrode acquired at a magnification five times lower than that used in Fig. 12.

Pos	IN	MID	OUT
Ref	5.5	5.5	5.7
MeOH/FT	5.0	3.7	3.4
CH4	8.8	7.3	5.8

or EDX in the inspected regions, suggesting that significant carbon deposition is unlikely under the tested conditions on the fuel electrode surfaces. To further verify this observation, Raman spectroscopy was performed on both the Ni-YSZ electrode and the Ni contact layer. Point Raman measurements were acquired at 20 positions on each region, and the resulting spectra were evaluated by calculating the mean spectrum and the corresponding standard deviation. No Raman bands characteristic of graphitic or amorphous carbon were detected between 1100 and 1600 cm^{-1} [77], confirming the SEM and EDX findings. Raman peaks observed at shifts below 750 cm^{-1} are most likely associated with lattice vibrations of the YSZ structure [78–80]. The corresponding Raman spectra are provided in Figure A.5 in Appendix A. This observation aligns with the calculated border of carbon deposition using HSC Chemistry 10 (© Metso [62]) for the in- and outlet composition under atmospheric pressure, which indicates carbon formation onset at 406/608 °C for Comp. MeOH/FT and 384/583 °C for Comp. CH4 as a guideline for carbon formation. These observations, together with thermodynamic calculations, indicate that under the investigated conditions carbon formation is unlikely to occur to an extent that would measurably affect the structural integrity of the Ni-YSZ fuel electrodes during long-term co-electrolysis.

Cross-sections

Cross-sectional SEM images of the cells are presented in Fig. 13. The cross-section of the reference cell (Fig. 13(a) and (d)) illustrates the complete cell architecture. Since the cell is fuel-electrode-supported, the fuel electrode forms the majority of the total thickness, providing the

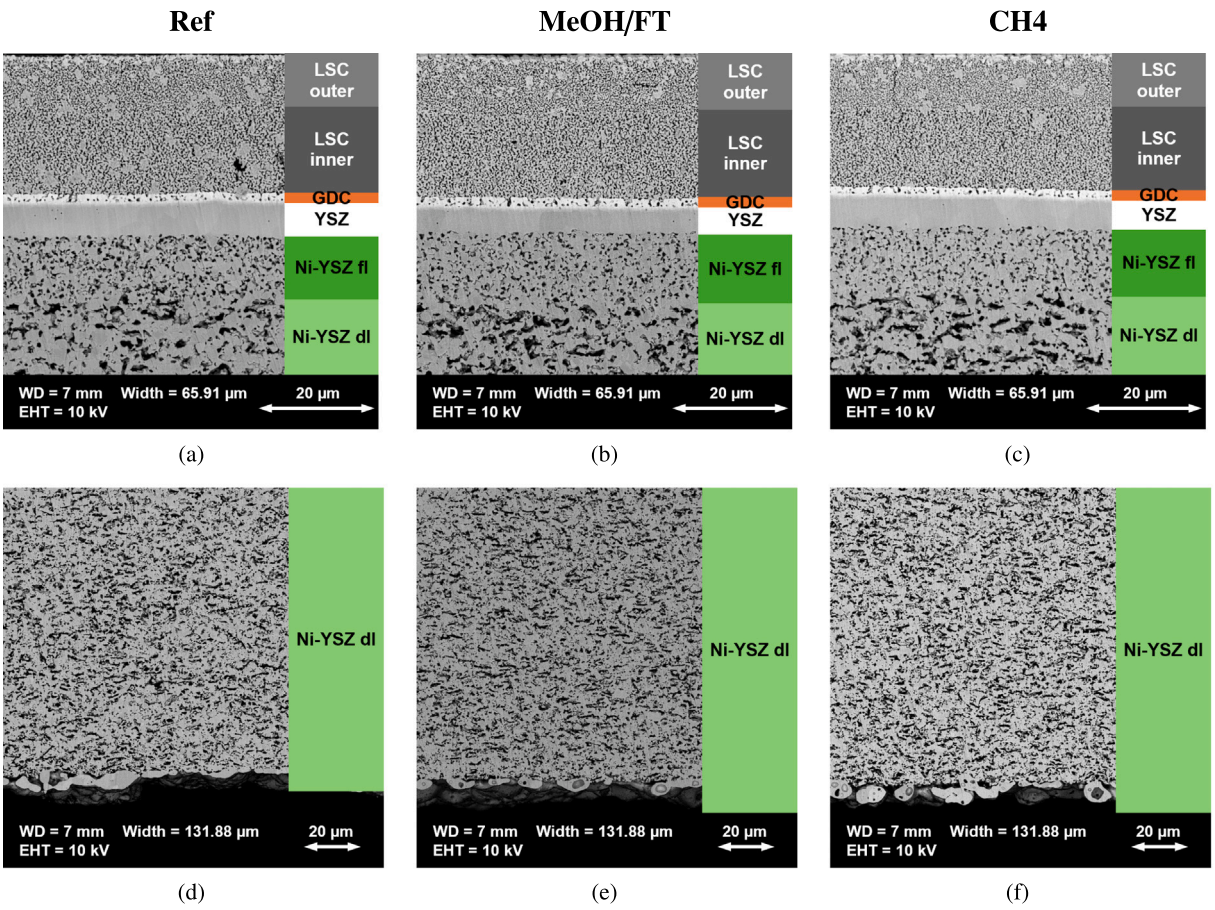

Fig. 13. SEM cross-section images of all cells at MID-position (WD-Working Distance, EHT-Electron High Tension): (a) initial state, (b) MeOH/FT, (c) CH4, (d) initial state-fuel electrode, (e) MeOH/FT-fuel electrode, and (f) CH4-fuel electrode.

Table 6
Calculated porosities (in %) derived from SEM cross-section images used in Fig. 13.

	LSC outer	LSC inner	Ni/YSZ fl	Ni/YSZ dl
Ref	20.0	20.1	18.6	23.2
MeOH/FT	19.9	20.9	17.0	25.7
CH4	13.4	16.5	11.3	22.2

required mechanical stability. It comprises two distinct Ni-YSZ layers with different porosities: (i) a diffusion layer (Ni-YSZ dl) with a porosity of 23.2% (see Table 6), which facilitates gas transport through the electrode, and (ii) a functional layer (Ni-YSZ fl) with a porosity of 18.6%, characterized by a higher density of triple-phase boundaries (TPBs), where gas, the ionic conductor (YSZ), and the electronic conductor (Ni) intersect, thereby enhancing electrochemical activity. At the bottom of Fig. 13(d), the previously observed Ni contact layer on top of the Ni-YSZ dl can be seen in cross-section. The electrolyte layer (YSZ) is located between the two electrodes, with a gadolinia-doped ceria (GDC) barrier layer added between the air electrode (LSC inner) and the electrolyte. This barrier layer prevents reactions between YSZ and La or Sr from the air electrode, which could otherwise lead to the formation of insulating secondary phases such as $La_2Zr_2O_7$ and $SrZrO_3$ [19]. Although it is difficult to distinguish two separate layers within the LSC in the reference cell, this distinction becomes more evident in cells after long-term operation. Therefore, the air electrode consists of an inner LSC layer with generally larger grains and an outer LSC layer with generally smaller grains; however, even larger grains are present in both layers. These larger grains reduce the porosity in the cross-sectional analysis in both layers, resulting in comparable porosities of 20.1% and 20.0% for the inner and outer LSC layers, respectively. The measured layer thicknesses are in good agreement with the manufacturer's specifications, yielding a total cell thickness of approximately 315 µm, comprising the air electrode including the GDC layer (~26 µm), the electrolyte (~6 µm), and the reduced fuel electrode (~283 µm).

Unexpectedly, in the reference cell (Ref, Fig. 13a), both the inner and outer LSC layers exhibited a mixture of small grains and larger agglomerated ones. Sr-rich and Pt-containing grains, previously identified in surface analyses, were also detected at the top of the LSC electrode. These likely form a thin surface layer that may act as a contact layer with reduced electrical resistance due to the presence of Pt. After long-term operation with Comp. MeOH/FT (Fig. 13b) or Comp. CH4 (Fig. 13c), the thickness of this surface layer increased slightly, indicating progressive Sr surface segregation and Pt diffusion from the contact mesh toward the electrode. In both operated cells, the agglomerated LSC grains within the inner LSC layer diminished or disappeared, resulting in a more homogeneous microstructure. The corresponding porosity was 20.9% for the cell operated for 280 h with Comp. MeOH/FT and 16.5% for the cell operated for 500 h with Comp. CH4. The slower change in porosity observed for Comp. MeOH/FT may be linked to differences in operating conditions, including the lower air flow rate, which could result in higher local O_2 partial pressures during electrolysis and thereby influence pore coarsening. However, because the two cells were operated for different durations and under different fuel compositions, the independent contribution of air-side conditions cannot be strictly isolated from the present results, although the observed microstructural trends remain consistent with such an influence. Similar trends were found in the outer LSC layer:

the porosity remained nearly unchanged for Comp. MeOH/FT (19.9%) but decreased notably for Comp. CH4 (13.4%). However, as the two cells were operated for different durations, these results might also suggest a time-dependent evolution of porosity under constant temperature and current density. Verifying such a correlation would require a systematic study with multiple cells tested for varying durations, which lies beyond the scope of the present work. In general, the temporal evolution of porosity in solid oxide cells has received limited attention. Most studies focus on delamination or secondary phase formation within the air electrode and report porosity values only for fresh and post-test samples, rather than monitoring its progression. For instance, Pretschuh et al. [58] quantified porosity after long-term operation but did not examine its evolution over time. Interestingly, no macroscopic delamination was observed in the inspected cross-sections in any of the cells at the LSC/GDC interface, commonly a critical failure mode in SOCs [81–83]. This suggests that the investigated operating conditions did not worsen LSC/GDC interfacial degradation during the tested long-term operation.

On the fuel electrode, the porosity of the diffusion layer (Ni-YSZ dl) increased to 25.7% in the cell operated with Comp. MeOH/FT (Fig. 13e). This increased porosity likely enhanced gas transport and removal toward the triple-phase boundary within the functional layer (Ni-YSZ fl) of the electrode (Fig. 13b). However, the porosity of the functional layer decreased to 17.0%, which would hinder gas flow and increase mass-transport resistance. The reduced number of pores along the Ni-YSZ fl/YSZ (electrode-electrolyte) interface may also account for the slight increase in diffusion-related losses (P_{LF}) observed over time in Fig. 7b). A comparable trend was observed in the cell operated with Comp. CH4 (Fig. 13c), where the porosity of the Ni-YSZ fl decreased further to 11.3%, corresponding to a similar gradual rise in diffusion losses (P_{LF}) over time in Fig. 10b). In this case, the porosity of the diffusion layer (Fig. 13f) also declined to 22.2%, likely as a consequence of the longer testing duration under Comp. CH4 operation. As already observed in the surface SEM analyses, no evidence of carbon deposition was found on any of the fuel electrodes. This finding is confirmed by the cross-sectional images of both the Ni-YSZ fl and Ni-YSZ dl layers. Supplementary areal EDX data for all fuel electrode layers and all tested cells are provided in Appendix A. To further verify the absence of carbon formation, Raman spectroscopy was performed on both the Ni-YSZ fl and Ni-YSZ dl regions. Point Raman measurements were acquired at 20 positions on Ni particles in each layer, and the resulting spectra were evaluated by calculating the mean spectrum and the corresponding standard deviation. No Raman bands characteristic of graphitic or amorphous carbon were detected between 1100 and 1600 cm^{-1} [77]. In some measurement positions, weak Raman peaks below 750 cm^{-1} were observed, which may be attributed to contributions from the YSZ structure when the measurement spot partially overlapped with the ceramic phase [78–80]. Due to their low intensity, these peaks do not affect the evaluation regarding the absence of carbon-related Raman bands. The corresponding Raman spectra are provided in Figure A.6 in Appendix A. Although the cell is fuel-electrode-supported, meaning that the Ni surface area is comparatively large, which typically increases the possibility for carbon deposition under CO- and hydrocarbon-containing atmospheres [20], no signs of carbon formation were detected after long-term operation. This suggests that both gas compositions did not accelerate carbon formation, even for Comp. MeOH/FT, which featured a relatively low steam-to-carbon ratio (S/C) of 1.38.

In the present study, no qualitative difference in the fuel-electrode degradation was observed between operation targeting $H_2/CO = 2$ (MeOH/FT) and $H_2/CO = 3$ (CH4). In both cases, Ni-YSZ coarsening in the functional layer was the dominant degradation feature, accompanied by a gradual reduction in porosity. No composition-specific degradation pathway could be identified. The more pronounced porosity reduction observed in the CH4 case may therefore be attributed primarily to the longer operation time rather than to the moderate difference in H_2O/CO_2 ratio. From a thermodynamic and kinetic perspective, however, an increase in the H_2O/CO_2 ratio during co-electrolysis can elevate the local oxygen chemical potential through the H_2O/H_2 equilibrium, shifting conditions closer to the Ni/NiO stability boundary and potentially enhancing Ni surface diffusion and agglomeration [16,52,84]. Steam has also been reported to accelerate Ni coarsening even under globally reducing conditions [26,85]. Nevertheless, Ni agglomeration is governed by the combined influence of temperature, current density, and full gas-phase equilibria (H_2O/H_2 and CO_2/CO), with temperature primarily controlling diffusion kinetics [25]. Under the present operating conditions (800 °C, identical current density), temperature and exposure time appear to have dominated the microstructural evolution more strongly than the targeted syngas composition.

4. Conclusion

In this study, long-term co-electrolysis experiments were conducted using two fuel-electrode-supported, industrial-sized commercial planar cells operated under syngas-representative gas compositions corresponding to methanol/Fischer-Tropsch synthesis (MeOH/FT) and methanation (CH4). A comprehensive diagnostic framework, combining voltage monitoring, polarization curves, fast EIS, DRT analysis, and electrode-temperature monitoring, together with post-mortem SEM/EDX and quantitative porosity evaluation (surface and cross-section, benchmarked against a reference cell), enabled direct correlation between electrochemical performance and microstructural evolution.

The key findings can be summarized as follows:

- *PtX-relevant long-term performance*: This study provides rare long-term performance and degradation-rate data for industrial-sized SOEC single cells under two PtX-relevant syngas conditions. Voltage degradation rates were 68.7 mV/1000 h for MeOH/FT (calculated over 228 h) and 27.3 mV/1000 h for CH4 (calculated over 470 h). Truncated evaluation of the CH4 case over matched shorter windows (up to 228–250 h) yielded lower early-time degradation rates, indicating a moderate increase in degradation rate at longer operating times. These results fill a critical gap in the literature regarding the durability of industrial-sized (large-area) cells under realistic co-electrolysis conditions.
- *Coupled electrochemical/microstructural evolution*: Two operating phases were identified in a long-term test: an initial improvement phase followed by degradation. The early enhancement was linked to Pt migration from the air-side contact mesh into the LSC, consistent with DRT peaks indicating reduced oxygen surface-exchange and charge-transfer losses, resulting in an early voltage decrease of up to 3.5%.
- *Fuel-electrode stability and dominant degradation mechanism*: The Ni-YSZ fuel electrodes showed a high degree of robustness against carbon under both, Comp. MeOH/FT and Comp. CH4, conditions. No carbon deposition and/or associated morphological changes were detected, and only the cell operated with Comp. CH4 showed Ni coarsening in the contact layer. The dominant long-term degradation mechanism on the fuel side was Ni-YSZ coarsening in the functional layer, accompanied by a gradual porosity decrease, while electrode-electrolyte interfaces remained intact. These findings suggest that operational strategies such as moderately reduced operating temperature may help slow coarsening-driven degradation.
- *Air-electrode sensitivity to air-flow conditions*: The air electrode exhibited pronounced sensitivity to local conditions, particularly under reduced air-flow in the MeOH/FT case. Pronounced Pt migration, Sr surface segregation, and formation of Pt/Sr secondary phases were accompanied by reduced surface porosity and partial surface degradation, while the LSC/GDC interface remained stable. Adequate air-flow management is therefore essential to minimize accelerated air-side degradation.

Taken together, these findings demonstrate that although both fuel compositions enable stable, carbon-free operation at 800 °C and 750 mA/cm^2, long-term degradation is governed by Ni-YSZ coarsening on the fuel side and Pt/Sr-related surface degradation on the air side, with air-flow rate playing a potentially important role. This work provides one of the first systematic assessments of degradation pathways in industrial-sized SOECs under syngas-relevant PtX conditions. Future research will examine alternative current-collector materials (e.g., gold to suppress initial improvement or stainless steel to emulate stack-operation), explore reduced-temperature operation as a strategy to mitigate coarsening-driven degradation, and perform systematic parametric studies in which the H_2O/CO_2 feed ratio and air flow rate are varied in a controlled manner to distinguish their respective contributions to degradation during co-electrolysis. Furthermore, the operating duration will be increased toward and beyond 1000 h to enable comprehensive lifetime assessment and long-term stability validation under PtX-relevant co-electrolysis conditions.

CRediT authorship contribution statement

Daniel Reiner: Writing–review & editing, Writing–original draft, Visualization, Validation, Software, Resources, Methodology, Investigation, Formal analysis, Data curation, Conceptualization. **Srđan Marković:** Methodology, Investigation. **Hartmuth Schröttner:** Investigation, Data curation. **Pavle Boškoski:** Software. **Christoph Hochenauer:** Writing–review & editing, Resources, Project administration, Funding acquisition. **Vanja Subotić:** Writing–review & editing, Supervision, Project administration, Funding acquisition.

Declaration of competing interest

The authors declare that they have no known competing financial interests or personal relationships that could have appeared to influence the work reported in this paper.

Acknowledgements

The authors gratefully acknowledge funding received as part of the CoGen project (within the HyCentA COMET Centre (grant ID 892427)). The COMET centre is funded within the COMET–Competence Centers for Excellent Technologies Program and funded by BMK, BMDW, the SFG, and the provinces of Styria, Upper Austria Tyrol and Vienna. The COMET Program is managed by FFG.

Appendix A. Supplementary data

Supplementary data for this article can be found online at doi:10.1016/j.apenergy.2026.128051.

Data availability

Data will be made available on request.

References

[1] IEA. Renewables 2024. Technical Report, IEA; 2024. https://www.iea.org/reports/renewables-2024. (accessed: 11 November 2025)
[2] IRENA. Record-Breaking annual growth in renewable power capacity. 2025. https://www.irena.org/News/pressreleases/2025/Mar/Record-Breaking-Annual-Growth-in-Renewable-Power-Capacity. (accessed: 11 November 2025).
[3] IRENA. Renewables in 2024: 5 key facts behind a Record-Breaking year. 2024. https://www.irena.org/News/articles/2025/Apr/Renewables-in-2024-5-Key-Facts-Behind-a-Record-Breaking-Year. (accessed: 11 November 2025).
[4] EMBER. Global electricity review 2025. Technical Report, EMBER; 2025. https://ember-energy.org/latest-insights/global-electricity-review-2025/. (accessed: 11 November 2025).
[5] Ferrete F, Molina A, González GMC, Moreno-Racero Á, Olmedo H, Iranzo A, Ferrete F, Molina A, González GMC, Moreno-Racero Á, Olmedo H, Iranzo A. Solid oxide electrolyzers process integration: a comprehensive review, Processes 2025, Vol. 13, 2025. https://doi.org/10.3390/PR13082656, 13.
[6] Liu Z, Hu J, Wu A, Lu Z, Guan W. Stability and energy consumption of solid oxide electrolysis cells under wide fluctuating and stable conditions. J Power Sources 2024;616:235113. https://doi.org/10.1016/J.JPOWSOUR.2024.235113
[7] Laguna-Bercero MA. Recent advances in high temperature electrolysis using solid oxide fuel cells: a review. J Power Sources 2012;203:4–16. https://doi.org/10.1016/J.JPOWSOUR.2011.12.019
[8] Fan L, Luo W, Fan Q, Hu Q, Jing Y, Chiu TW, Lund PD. Status and outlook of solid electrolyte membrane reactors for energy, chemical, and environmental applications. Chem Sci 2025;16:6620–87. https://doi.org/10.1039/d4sc08300h
[9] Wang Y, Liu T, Lei L, Chen F. High temperature solid oxide h_2o/CO_2 CO-electrolysis for syngas production. Fuel Process Technol 2017;161:248–58. https://doi.org/10.1016/J.FUPROC.2016.08.009
[10] Ostadi M, Rytter E, Hillestad M. Boosting carbon efficiency of the biomass to liquid process with hydrogen from power: the effect of h2/CO ratio to the Fischer-Tropsch reactors on the production and power consumption. Biomass and Bioenergy 2019;127:105282. https://doi.org/10.1016/J.BIOMBIOE.2019.105282
[11] Rabah AA. Optimization of syngas quality for Fischer-Tropsch synthesis. J Energy 2023;2023:1842187. https://doi.org/10.1155/2023/1842187
[12] Machado CFR, Medeiros JLD, Araújo OFQ, Alves RMB. A comparative analysis of methanol production routes: synthesis gas versus CO_2 hydrogenation. In: Proceedings of the 2014 international conference on industrial engineering and operations management; 2014. p. 2981–90. https://ieomsociety.org/ieom2014/pdfs/294.pdf.
[13] Baratti R, Bareschino P, Stellato F, Caravella A, Grosso M, Mancusi E, Tronci S, Leonzio G. Analysis of methanol production from bio-syngas through an innovative reactor. Chem Eng Trans 2025;117:91–6. https://doi.org/10.3303/CET25117016
[14] Mebrahtu C, Nohl M, Dittrich L, Foit SR, de Haart LG, Eichel RA, Palkovits R. Integrated Co-Electrolysis and syngas methanation for the direct production of synthetic natural gas from CO_2 and h_2o. Chemsuschem 2021;14:2295–302. https://doi.org/10.1002/CSSC.202002904
[15] Cheng C, Shen D, Xiao R, Wu C. Methanation of syngas (h2/CO) over the different ni-based catalysts. Fuel 2017;189:419–27. https://doi.org/10.1016/J.FUEL.2016.10.122
[16] Hauch A, Ebbesen SD, Jensen SH, Mogensen M. Solid oxide electrolysis cells: microstructure and degradation of the ni/Yttria-Stabilized zirconia electrode. J Electrochem Soc 2008;155:B1184. https://doi.org/10.1149/1.2967331
[17] Tao Y, Ebbesen SD, Mogensen MB. Degradation of solid oxide cells during co-electrolysis of steam and carbon dioxide at high current densities. J Power Sources 2016;328:452–62. https://doi.org/10.1016/J.JPOWSOUR.2016.08.055
[18] Wolf SE, Vibhu V, Tröster E, Vinke IC, Eichel RA, de Haart LG. Steam electrolysis VS. Co-Electrolysis: mechanistic studies of Long-Term solid oxide electrolysis cells. Energies 2022;15:5449. https://doi.org/10.3390/EN15155449/S1
[19] Wang Y, Li W, Ma L, Li W, Liu X. Degradation of solid oxide electrolysis cells: phenomena, mechanisms, and emerging mitigation strategies—a review. J Mater Sci Technol 2020;55:35–55. https://doi.org/10.1016/J.JMST.2019.07.026
[20] Zong S, Zhao X, Jewell LL, Zhang Y, Liu X. Advances and challenges with SOEC high temperature CO-electrolysis of CO_2/h_2o: materials development and technological design. Carbon Capture Sci Technol 2024;12:100234. https://doi.org/10.1016/J.CCST.2024.100234
[21] Rao M, Sun X, Hagen A. Durability of solid oxide electrolysis stack under dynamic load cycling for syngas production. J Power Sources 2020;451:227781. https://doi.org/10.1016/J.JPOWSOUR.2020.227781
[22] Kamkeng AD, Wang M. Long-term performance prediction of solid oxide electrolysis cell (SOEC) for CO_2/h_2o CO-electrolysis considering structural degradation through modelling and simulation. Chem Eng J 2022;429:132158. https://doi.org/10.1016/J.CEJ.2021.132158
[23] Xi C, Sang J, Wu A, Yang J, Qi X, Guan W, Wang J, Singhal SC. Electrochemical performance and durability of flat-tube solid oxide electrolysis cells for h_2o/CO_2 CO-electrolysis. Int J Hydrog Energy 2022;47:10166–74. https://doi.org/10.1016/J.IJHYDENE.2022.01.105
[24] Tong J, Ni N, Zhou B, Yang C, Reddy KM, Tu H, Liu Y, Tan Z, Xiang L, Li H, Zhou X, Zhang Y, Li Y, Zhang H, Zhu L, Huang Z. Toward high CO selectivity and oxidation resistance solid oxide electrolysis cell with High-Entropy alloy. ACS Catal 2024;14:2897–907. https://doi.org/10.1021/acscatal.3c05972
[25] Yang S, Gao J, Trini M, Angelis SD, Jørgensen PS, Bowen JR, Zhang L, Chen M. Ni coarsening in ni-yttria stabilized zirconia electrodes: three-dimensional quantitative phase-field simulations supported by ex-situ ptychographic nano-tomography. Acta Mater 2023;246:118708. https://doi.org/10.1016/J.ACTAMAT.2023.118708
[26] Mogensen MB, Hauch A, Sun X, Chen M, Tao Y, Ebbesen SD, Hansen KV, Hendriksen PV. Relation between ni particle shape change and ni migration in ni–YSZ electrodes – a hypothesis. Fuel Cells 2017;17:434–41. https://doi.org/10.1002/FUCE.201600222;CTYPE:STRING:JOURNAL
[27] Vibhu V, Vinke IC, Zaravelis F, Neophytides SG, Niakolas DK, Eichel RA, de Haart LG. Performance and degradation of Electrolyte-Supported single cell composed of Mo-Au-Ni/GDC fuel electrode and LSCF oxygen electrode during high temperature steam electrolysis. Energies 2022;15. https://doi.org/10.3390/EN15082726/S1
[28] Hyeon-Ye J, Joong YK, Jong-Ho L, Yong-Chae C, Jongsup H. Long-Term stability for Co-Electrolysis of CO_2/steam assisted by Catalyst-Infiltrated solid oxide cells. Journal of the Korean Ceramic Society 2018;50–4. https://doi.org/10.4191/kcers.2018.55.1.09
[29] Unachukwu ID, Vibhu V, Vinke IC, Eichel RA, de Haart LG. Electrochemical and degradation behaviour of single cells comprising ni-GDC fuel electrode under high temperature steam- and co-electrolysis conditions. J Power Sources 2023;556:232436. https://doi.org/10.1016/J.JPOWSOUR.2022.232436
[30] Elcogen AS. Solid oxide electrolysis cells. 2024. https://elcogen.com/products/solid-oxide-electrolysis-cells/ [accessed: 31 July 2025].
[31] Reiner D, Marković S, Schröttner H, Hochenauer C, Subotić V. Electrochemical investigation of the influence of gas compositions on industrial-sized fuel electrode

supported single cells under CO- and CO_2-electrolysis conditions. J Co_2 Util 2025;99:103152. https://doi.org/10.1016/J.JCOU.2025.103152
[32] Höber M, Königshofer B, Schröttner H, Fitzek H, Menzler NH, Hochenauer C, Subotić V. Experimental identification of the impact of direct internal and external methane reforming on SOFC by detailed online monitoring and supporting measurements. J Power Sources 2023;581:233449. https://doi.org/10.1016/J.JPOWSOUR.2023.233449
[33] Königshofer B, Pongratz G, Nusev G, Boškoski P, Höber M, Juričić Đ, Kusnezoff M, Trofimenko N, Schröttner H, Hochenauer C, Subotić V. Development of test protocols for solid oxide electrolysis cells operated under accelerated degradation conditions. J Power Sources 2021;497:229875. https://doi.org/10.1016/J.JPOWSOUR.2021.229875
[34] Stoeckl B, Subotić V, Preininger M, Schroettner H, Hochenauer C. SOFC operation with carbon oxides: experimental analysis of performance and degradation. Electrochim Acta 2018;275:256–64. https://doi.org/10.1016/J.ELECTACTA.2018.04.036
[35] Stoeckl B, Subotić V, Reichholf D, Schroettner H, Hochenauer C. Extensive analysis of large planar SOFC: operation with humidified methane and carbon monoxide to examine carbon deposition based degradation. Electrochim Acta 2017;256:325–36. https://doi.org/10.1016/J.ELECTACTA.2017.09.026
[36] ABB Automation Products GmbH. Continuous gas analyzers - advance optima and EasyLine series - el3020. 2025. https://new.abb.com/products/measurement-products/analytical/advance-optima-and-easyline-series/el3000 [accessed: 31 July 2025].
[37] Wiegleb G. Gasmesstechnik in theorie und praxis. Springer Fachmedien Wiesbaden; 2022. https://doi.org/10.1007/978-3-658-35278-3
[38] I.E.C. ITECH LTD. Wide range high power DC power supply | it6500-welcome to ITECH. 2025. https://www.itechate.com/en/product/dc-power-supply/IT6500.html [accessed: 31 July 2025].
[39] Boškoski P, Debenjak A, Boshkoska BM ed. Fast electrochemical impedance spectroscopy. 1 ed. Springer International Publishing; 2017. https://doi.org/10.1007/978-3-319-53390-2. http://link.springer.com/10.1007/978-3-319-53390-2.
[40] Nusev G, Morel B, Mougin J, Juričić Đ, Boškoski P. Condition monitoring of solid oxide fuel cells by fast electrochemical impedance spectroscopy: a case example of detecting deficiencies in fuel supply. J Power Sources 2021;489:229491. https://doi.org/10.1016/J.JPOWSOUR.2021.229491
[41] Subotić V, Königshofer B, Juričić Đ, Kusnezoff M, Schröttner H, Hochenauer C, Boškoski P. Detailed insight into processes of reversible solid oxide cells and stacks using DRT analysis. Energy Convers Manag 2020;226:113509. https://doi.org/10.1016/J.ENCONMAN.2020.113509
[42] Mütter F, Boškoski P, Megel S, Hochenauer C, Subotić V. Optimising solid oxide cells for co-electrolysis operation: parameter interactions and efficiency gains at industrial scale. Appl Energy 2025;396:126229. https://doi.org/10.1016/J.APENERGY.2025.126229
[43] Mütter F, Boškoski P, Megel S, Hochenauer C, Subotić V. Operating sensitivities for steam versus co-electrolysis on a commercial solid-oxide electrolysis stack with Power-to-X implications. Fuel 2026;411:137992. https://doi.org/10.1016/J.FUEL.2025.137992
[44] Höber M, Königshofer B, Schröttner H, Fitzek H, Menzler NH, Hochenauer C, Subotić V. Experimental identification of the impact of direct internal and external methane reforming on SOFC by detailed online monitoring and supporting measurements. J Power Sources 2023;581:233449. https://doi.org/10.1016/J.JPOWSOUR.2023.233449
[45] Yan J, Chen H, Dogdibegovic E, Stevenson JW, Cheng M, Zhou XD. High-efficiency intermediate temperature solid oxide electrolyzer cells for the conversion of carbon dioxide to fuels. J Power Sources 2014;252:79–84. https://doi.org/10.1016/J.JPOWSOUR.2013.11.047
[46] Yan Y, Fang Q, Blum L, Lehnert W. Performance and degradation of an SOEC stack with different cell components. Electrochim Acta 2017;258:1254–61. https://doi.org/10.1016/J.ELECTACTA.2017.11.180
[47] Huang Z, Qi H, Zhao Z, Shang L, Tu B, Cheng M. Efficient CO_2 electroreduction on a solid oxide electrolysis cell with la0.6sr0.4co0.2fe0.8o3-δ-gd0.2ce0.8o2-δ infiltrated electrode. J Power Sources 2019;434:226730. https://doi.org/10.1016/J.JPOWSOUR.2019.226730
[48] Park KY, Lee T, Wang W, Li H, Chen F. High-performance ruddlesden–popper perovskite oxide with in situ exsolved nanoparticles for direct CO_2 electrolysis. J Mater Chem A 2023;11:21354–64. https://doi.org/10.1039/D3TA04122K
[49] Yang Y, Tong X, Hauch A, Sun X, Yang Z, Peng S, Chen M. Study of solid oxide electrolysis cells operated in potentiostatic mode: effect of operating temperature on durability. Chem Eng J 2021;417:129260. https://doi.org/10.1016/J.CEJ.2021.129260
[50] Pan Z, Liu Q, Ni M, Lyu R, Li P, Chan SH. Activation and failure mechanism of la0.6sr0.4co0.2fe0.8o3-δ AIR electrode in solid oxide electrolyzer cells under high-current electrolysis. Int J Hydrog Energy 2018;43:5437–50. https://doi.org/10.1016/J.IJHYDENE.2018.01.181
[51] Hjalmarsson P, Sun X, Liu YL, Chen M. Durability of high performance ni–yttria stabilized zirconia supported solid oxide electrolysis cells at high current density. J Power Sources 2014;262:316–22. https://doi.org/10.1016/J.JPOWSOUR.2014.03.133
[52] Sun X, Hendriksen PV, Mogensen MB, Chen M. Degradation in solid oxide electrolysis cells during long term testing. Fuel Cells 2019;19:740–7. https://doi.org/10.1002/FUCE.201900081
[53] Orlić M, Reiner D, Radowski D, Montinaro D, Hochenauer C, Subotić V. Dual pathways for refinery off-gas processing: comparative analysis of steam reforming and co-electrolysis. Energy Convers Manag 2025;346:120356. https://doi.org/10.1016/J.ENCONMAN.2025.120356
[54] Graves C, Ebbesen SD, Mogensen M. CO-electrolysis of CO_2 and h_2o in solid oxide cells: performance and durability. Solid State Ion 2011;192:398–403. https://doi.org/10.1016/J.SSI.2010.06.014
[55] Königshofer B, Höber M, Nusev G, Boškoski P, Juričić Đ, Margaritis N, Hochenauer C, Subotić V. Towards strategies to mitigate degradation and regenerate performance of a solid oxide electrolyzer during co-electrolysis operation. J Power Sources 2023;556:232404. https://doi.org/10.1016/J.JPOWSOUR.2022.232404
[56] Schindelin J, Rueden CT, Hiner MC, Eliceiri KW. The ImageJ ecosystem: an open platform for biomedical image analysis. Molecular Reproduction and Development 2015;82:518–29. https://doi.org/10.1002/mrd.22489
[57] Rueden CT, Schindelin J, Hiner MC, DeZonia BE, Walter AE, Arena ET, Eliceiri KW. Imagej2: ImageJ for the next generation of scientific image data. BMC Bioinform 2017;18:1–26. https://doi.org/10.1186/S12859-017-1934-z
[58] Pretschuh P, Egger A, Brunner R, Bucher E. Electrochemical and microstructural characterization of the high-entropy perovskite $LA_{0.2}pr_{0.2}ND_{0.2}sm_{0.2}SR_{0.2}CoO_{3-\delta}$ for solid oxide cell AIR electrodes. Fuel Cells 2023;23:377–86. https://doi.org/10.1002/FUCE.202300036;WGROUP:STRING:PUBLICATION
[59] Savitzky A, Golay MJ. Smoothing and differentiation of data by simplified least squares procedures. Anal Chem 1964;36:1627–39. https://doi.org/10.1021/AC60214A047/ASSET/AC60214A047
[60] Luo J, Ying K, Bai J. Savitzky–golay smoothing and differentiation filter for even number data. Signal Process 2005;85:1429–34. https://doi.org/10.1016/J.SIGPRO.2005.02.002
[61] O'Brien JE, Stoots CM, Herring JS, Hartvigsen JJ. High-Temperature co-electrolysis of steam and carbon dioxide for direct production of syngas; equilibrium model and Single-Cell tests. In: Fifth international fuel cell science, engineering, and technology conference. Idaho National Lab. (INL), Idaho Falls, ID (United States); 2007. p. 1–9. https://www.osti.gov/biblio/924520.
[62] Metso. HSC Chemistry 10 [software]. Metso Finland Oy; 2025.
[63] Suwanwarangkul R, Croiset E, Fowler MW, Douglas PL, Entchev E, Douglas MA. Performance comparison of fick's, dusty-gas and stefan–maxwell models to predict the concentration overpotential of a SOFC anode. J Power Sources 2003;122:9–18. https://doi.org/10.1016/S0378-7753(02)00724-3
[64] Ebbesen SD, Mogensen M. Electrolysis of carbon dioxide in solid oxide electrolysis cells. J Power Sources 2009;193:349–58. https://doi.org/10.1016/J.JPOWSOUR.2009.02.093
[65] Jensen SH, Larsen PH, Mogensen M. Hydrogen and synthetic fuel production from renewable energy sources. Int J Hydrog Energy 2007;32:3253–7. https://doi.org/10.1016/J.IJHYDENE.2007.04.042
[66] Zhao B, Tong Y, Zhao Y, Yang T, Yang F, Hu Q, Zhao C. Preparation of ultrafine $sm_{0.2}CE_{0.8}o_{1.9}$ powder by a novel solid state reaction and fabrication of dense $sm_{0.2}CE_{0.8}o_{1.9}$ electrolyte film. Ceram Int 2015;41:9686–91. https://doi.org/10.1016/J.CERAMINT.2015.04.037
[67] Lu J, Hu Y, Zhang M, Hu Q, Wu J. Optimization of PT infiltrated $SR_2fe_{2-x}mo_xo_{6-\delta}CE_{0.8}sm_{0.2}o_{1.9}$ oxygen electrode for reversible solid oxide cell and CH_4-assisted electrolysis process. Int J Hydrog Energy 2024;55:786–95. https://doi.org/10.1016/J.IJHYDENE.2023.11.247
[68] Hwang HJ, Moon JW, Lee S, Lee EA. Electrochemical performance of LSCF-based composite cathodes for intermediate temperature SOFCs. J Power Sources 2005;145:243–8. https://doi.org/10.1016/J.JPOWSOUR.2005.02.063
[69] Boukamp BA, Hildenbrand N, Bouwmeester HJ, Blank DH. Impedance of thin film cathodes: thickness and current collector dependence. Solid State Ion 2015;283:81–90. https://doi.org/10.1016/J.SSI.2015.10.013
[70] Simner SP, Anderson MD, Pederson LR, Stevenson JW. Performance variability of LA(SR)FeO_3 SOFC cathode with PT, ag, and au current collectors. J Electrochem Soc 2005;152:A1851. https://doi.org/10.1149/1.1995687/PDF
[71] Laurencin J, Hubert M, Sanchez DF, Pylypko S, Morales M, Morata A, Morel B, Montinaro D, Lefebvre-Joud F, Siebert E. Degradation mechanism of $LA_{0.6}SR_{0.4}CO_{0.2}FE_{0.8}o_{3-\delta}/GD_{0.1}CE_{0.9}o_{2-\delta}$ composite electrode operated under solid oxide electrolysis and fuel cell conditions. Electrochim Acta 2017;241:459–76. https://doi.org/10.1016/J.ELECTACTA.2017.05.011
[72] Oh D, Gostovic D, Wachsman ED. Mechanism of $LA_{0.6}SR_{0.4}CO_{0.2}FE_{0.8}o_3$ cathode degradation. J Mater Res 2012;27:1992–9. https://doi.org/10.1557/JMR.2012.222
[73] Chen Y, Téllez H, Burriel M, Yang F, Tsvetkov N, Cai Z, McComb DW, Kilner JA, Yildiz B. Segregated Chemistry and structure on (001) and (100) surfaces of $(la_{1-x}sr_x)_2CoO_4$ override the crystal anisotropy in oxygen exchange kinetics. Chem Mater 2015;27:5436–50. https://doi.org/10.1021/ACS.CHEMMATER.5B02292
[74] Mutoro E, Crumlin EJ, Pöpke H, Luerssen B, Amati M, Abyaneh MK, Biegalski MD, Christen HM, Gregoratti L, Janek J, Shao-Horn Y. Reversible compositional control of oxide surfaces by electrochemical potentials. J Phys Chem Lett 2011;3:40–4. https://doi.org/10.1021/JZ201523Y
[75] Porotnikova N, Osinkin D. Segregation and interdiffusion processes in perovskites: a review of recent advances. J Mater Chem A 2024;12:2620–46. https://doi.org/10.1039/D3TA06708D
[76] Finsterbusch M, Lussier A, Schaefer JA, Idzerda YU. Electrochemically driven cation segregation in the mixed conductor $LA_{0.6}SR_{0.4}CO_{0.2}FE_{0.8}o_{3-\delta}$. Solid State Ion 2012;212:77–80. https://doi.org/10.1016/J.SSI.2012.02.006
[77] Ferrari A, Robertson J. Interpretation of Raman spectra of disordered and amorphous carbon. Phys Rev B 2000;61:14095. https://doi.org/10.1103/PhysRevB.61.14095
[78] Zhu W, Nakashima S, Marin E, Gu H, Pezzotti G. Microscopic mapping of dopant content and its link to the structural and thermal stability of yttria-stabilized

zirconia polycrystals. Journal of Materials Science 2019 55:2 2019;55:524–34. https://doi.org/10.1007/s10853-019-04080-9

[79] Ciszak C, Mermoux M, Gutierrez G, Leprêtre F, Duriez C, Popa I, Fayette L, Chevalier S. Raman spectra analysis of ZrO_2 thermally grown on zircaloy substrates irradiated with heavy ION: effects of oxygen isotopic substitution. J Raman Spectrosc 2019;50:425–35. https://doi.org/10.1002/jrs.5513

[80] Margueron S, Bartasyte A. Temperature-dependent resonant Raman scattering of yttria doped zirconia phases in thermal barrier coatings. J Eur Ceram Soc 2024;44:419–25. https://doi.org/10.1016/j.jeurceramsoc.2023.08.046

[81] Virkar AV. Mechanism of oxygen electrode delamination in solid oxide electrolyzer cells. Int J Hydrog Energy 2010;35:9527–43. https://doi.org/10.1016/J.IJHYDENE.2010.06.058

[82] Sreedhar I, Agarwal B, Goyal P, Agarwal A. An overview of degradation in solid oxide fuel cells-potential clean power sources. Journal of Solid State Electrochemistry 2020 24:6 2020;24:1239–70. https://doi.org/10.1007/S10008-020-04584-4

[83] Pan Z, Liu Q, Yan Z, Jiao Z, Bi L, Chan SH, Zhong Z. On the delamination of AIR electrodes of solid oxide electrolysis cells: a mini-review. Electrochem Commun 2022;137:107267. https://doi.org/10.1016/J.ELECOM.2022.107267

[84] Yokokawa H, Tu H, Iwanschitz B, Mai A. Fundamental mechanisms limiting solid oxide fuel cell durability. J Power Sources 2008;182:400–12. https://doi.org/10.1016/j.jpowsour.2008.02.016

[85] Holzer L, Münch B, Iwanschitz B, Cantoni M, Hocker T, Graule T. Electrical conductivity of ni–YSZ composites: degradation due to ni particle growth. Solid State Ion 2011;189:82–90. https://doi.org/10.1016/j.jpowsour.2010.08.006